Biophysical Journal
Article

Allosteric Mechanisms of Nonadditive Substituent Contributions to Protein-Ligand Binding

Stephen Boulton,[1] Katherine Van,[1] Bryan VanSchouwen,[2] Jerry Augustine,[1] Madoka Akimoto,[2]
and Giuseppe Melacini[1,2,*]
[1]Department of Biochemistry and Biomedical Sciences and [2]Department of Chemistry and Chemical Biology, McMaster University, Hamilton, Canada

ABSTRACT Quantifying chemical substituent contributions to ligand-binding free energies is challenging due to nonadditive effects. Protein allostery is a frequent cause of nonadditivity, but the underlying allosteric mechanisms often remain elusive. Here, we propose a general NMR-based approach to elucidate such mechanisms and we apply it to the HCN4 ion channel, whose cAMP-binding domain is an archetypal conformational switch. Using NMR, we show that nonadditivity arises not only from concerted conformational transitions, but also from conformer-specific effects, such as steric frustration. Our results explain how affinity-reducing functional groups may lead to affinity gains if combined. Surprisingly, our approach also reveals that nonadditivity depends markedly on the receptor conformation. It is negligible for the inhibited state but highly significant for the active state, opening new opportunities to tune potency and agonism of allosteric effectors.

SIGNIFICANCE Understanding the allosteric mechanisms underlying the nonadditivity of substituent contributions to the free energy of protein-ligand binding is a central challenge in biophysical chemistry. Yet, a general methodology to investigate such mechanisms is still lacking, especially for inherently dynamic systems that function as allosteric switches, alternating between inhibition competent and incompetent states. As a first step toward filling this gap, here, we present an NMR-based approach to dissect the allosteric driving forces of substituent nonadditivity. When applied to the HCN4 ion channel, this approach reveals that the determinants of binding nonadditivity include not only a single concerted two-state transition, but also conformation-dependent allosteric frustration.

INTRODUCTION

Understanding how ligand substituents control the free energy of binding is a central challenge in chemistry (1–5). One of the simplest approaches to quantify substituent contributions to the binding free energy relies on the principle of thermodynamic additivity (6–9). According to it, the ligand-binding free energy change caused by a double substitution is the sum of the changes elicited by the two single substitutions, provided that the two substituents act independently. However, substituents are often not independent and therefore the respective contributions to macromolecule-ligand-binding free energies are nonadditive (10,11). The difference between the change in binding free energy arising from a double substitution and the sum of the changes caused by the two single substitutions is the coupling free energy (Fig. 1, *a* and *b*; (8–11)) and is calculated as:

$$\Delta G_{coupling,AB} = -RT \ln \gamma_{Exp}, \tag{1}$$

with

$$\gamma_{Exp} \equiv \frac{K_{AB}K_S}{K_A K_B}, \tag{2}$$

where K_{AB}, K_S, K_A, and K_B are the respective association constants measured for the P:S$_{AB}$, P:S, P:S$_A$, and P:S$_B$ complexes, which define a double-ligand cycle (Fig. 1 *a*; (11)). Similar to the Q factor originally utilized to quantify the coupling between two different ligands (12,13), when $\gamma_{Exp} = 1$, full additivity applies (Fig. S1 *a*), whereas $\gamma_{Exp} > 1$ (<1) points to positive (negative) cooperativity between the A and B functional groups. Furthermore, if γ_{Exp} is within the $[e^{-1}, e]$ range, $|\Delta G_{coupling,AB}|$ does not exceed the thermal room temperature (RT) benchmark (~0.6 kcal/mol) and therefore the nonadditivity is considered marginal, even

---

Submitted May 20, 2020, and accepted for publication July 6, 2020.

*Correspondence: melacin@mcmaster.ca

Editor: Elizabeth Komives.

https://doi.org/10.1016/j.bpj.2020.07.038

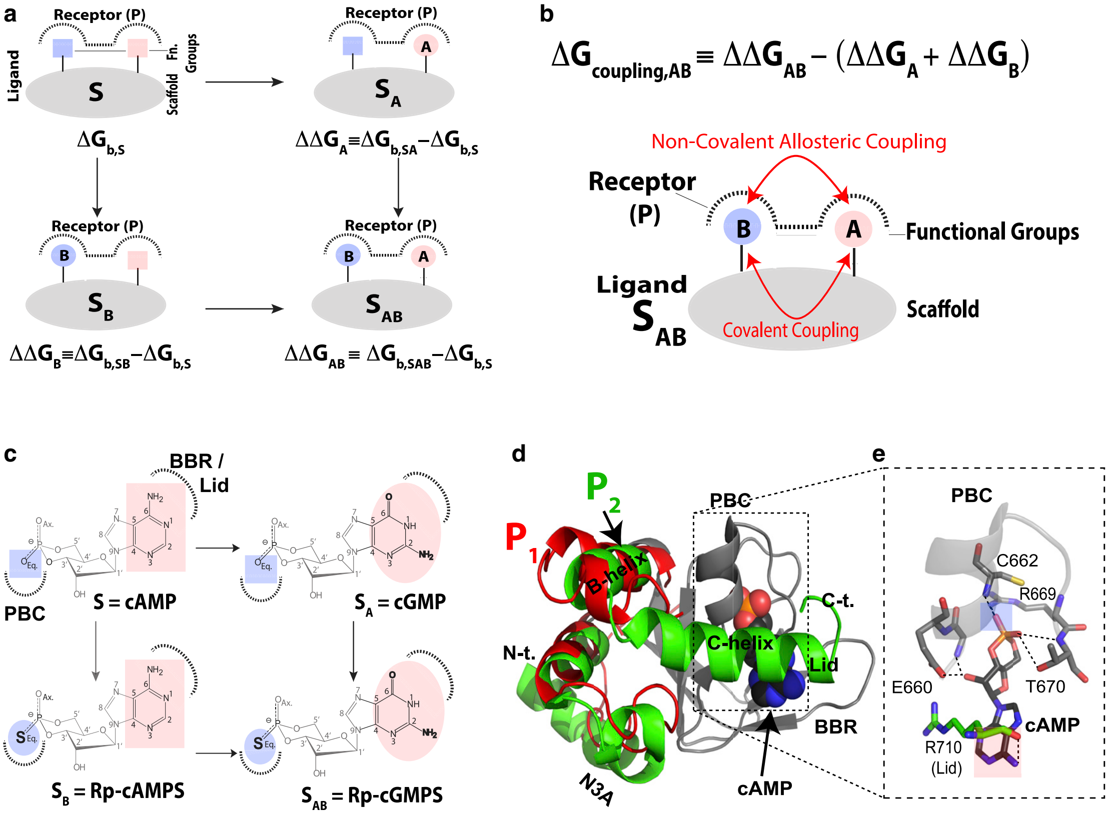

FIGURE 1 Nonadditivity between two ligand substituents as defined by double-ligand cycles. (*a*) General double-ligand cycle for a ligand composed of a scaffold or linker S (*gray*) and two substituents A (*pink*) and B (*blue*). The cycle includes four protein complexes in which the receptor (P) binds either S, the single-substituted ligands (*i.e.* S_A or S_B), or the double-substituted ligand S_{AB}. Dotted lines denote binding sites in P. $\Delta G_{b,S}$ is the binding free energy for ligand S, whereas $\Delta\Delta G_A$ is defined as the contribution to binding arising from substituent A in ligand S_A. Similar definitions apply to S_B and S_{AB}. If modifications A and B are independent, then $\Delta\Delta G_{AB} = \Delta\Delta G_A + \Delta\Delta G_B$, which is the equation defining binding additivity (Fig. S1 a). (*b*) Definition of the coupling free energy between substituents A and B ($\Delta G_{coupling,AB}$) and a scheme illustrating the covalent and/or noncovalent double nature of such coupling. (*c*) Example of the double-ligand cycle including the cyclic nucleotide monophosphates (cNMPs) cAMP, the phosphorothioate Rp-cAMPS, cGMP, and Rp-cGMPS. (*d*) Autoinhibitory and active conformations accessed by the cNMP-binding domain (CNBD) of HCN4 in the apo and cAMP-bound forms (PDB: 2MNG and PDB: 3OTF; denoted here as P_1 and P_2, respectively). The invariant β-subdomain is shown as a gray cartoon, whereas the more dynamic α-subdomain is depicted in red (apo) or green (cAMP-bound). Key structural motifs are labeled, including the phosphate-binding cassette (PBC), the base-binding region (BBR), and the N3A. (*e*) Expanded view of the PBC and part of the lid region of the HCN4 CNBD, highlighting key interactions of these regions with cAMP. Hydrogen bonds are shown as dashed lines. To see this figure in color, go online.

when γ_{Exp} differs from unity beyond experimental uncertainty.

The binding free energy nonadditivity arising from the coupling between substituents A and B severely limits the accuracy of several inherently linear docking scoring functions and classical quantitative structure activity relationship models (9–11,14). Hence, understanding the mechanisms underlying the cooperativity between simultaneous ligand modifications is crucial for drug design as well as computational and structural biology.

The coupling between substituents A and B may arise covalently (e.g., inductive or electromeric "through-ligand" effects; Fig. 1 *b*) or as the result of noncovalent changes in the protein and/or ligand (e.g., allosteric conformational changes in the protein receptor P, changes in ligand/protein interactions and/or solvation). Although covalent couplings have been extensively investigated, less is known about the noncovalent mechanisms underlying the coupling between ligand substituents (10,11).

Structural dynamics has been hypothesized to be one of the main noncovalent determinants of substituent couplings (9). Qualitative evidence in support of this hypothesis comes primarily from the comparative analysis of crystal structure B-factors for the complexes formed by a congeneric series of thrombin inhibitors (9). However, the allosteric mechanisms at the basis of nonadditive substituent contributions to binding free energies have not been fully investigated.

Here, using NMR spectroscopy, we elucidate the allosteric mechanisms underlying substituent nonadditivity in an archetypal ligand-dependent conformational switch (15), i.e., the cyclic-nucleotide (cNMP)-binding domain (CNBD) of the hyperpolarization-activated and cNMP-gated ion channel isoform 4 (HCN4; Fig. 1, *c–e*). The cNMP-dependent gating of HCN4 is critical to control basal heart rates (16), and similar allosteric switches regulate signal transduction pathways and enzymatic catalysis (15,17–36).

The CNBDs adopt a conserved architecture with a contiguous and relatively rigid β-subdomain composed of an eight-stranded β-barrel, as well as a noncontiguous and dynamic α-subdomain that includes an N-terminal helical bundle, denoted as the N-terminal three-helix bundle (N3A) motif, and two C-terminal helices, referred to as B and C (Fig. 1 *d*; (15,37,38)). The β-subdomain includes the phosphate-binding cassette (PBC) and the base-binding region (BBR), where the cNMP docks and recruits through its base the C-helix as a lid (Fig. 1 *d*). The closure of the lid over the cNMP base drives a conformational change in the α-subdomain from an autoinhibitory state, in which the N3A is proximal to the β-subdomain ("N3A in" topology), to an active state, in which the N3A is displaced away from the β-barrel ("N3A out" topology).

The apo CNBD dynamically samples both autoinhibitory and active conformations, denoted here as P_1 and P_2 (Fig. 1 *d*), which interconvert in the fast exchange regime, as previously shown (15). cAMP-binding selects and stabilizes the active state (26,39), whereas cAMP analogs modulate the position of the autoinhibitory versus active $P_1 \Leftrightarrow P_2$ equilibrium. Such modulations correlate with the cNMP-dependent changes in activation voltages ($\Delta V_{1/2}$) measured by electrophysiology for integral full-length ion channels (15). The linkage between the autoinhibitory $P_1 \Leftrightarrow P_2$ and ligand-binding equilibria of the CNBD is best described by a classical four-state thermodynamic cycle, where the coupling between the two equilibria depends on the ratio between the state-specific association constants K_{1j} and K_{2j} (Fig. S1 b), which define the P_1 versus P_2 state-selectivity of a given ligand S_j (i.e., S, S_A, S_B, or S_{AB} in the double-ligand cycle of Fig. 1 *a*).

In the case of HCN4 investigated here, the scaffold ligand S is the endogenous allosteric effector cAMP, whereas the other ligands are built by introducing either a phosphate substitution (e.g., equatorial exocyclic oxygen to sulfur in Rp-cAMPS), a base substitution (e.g., adenine to guanine in cGMP), or a combination of the two (e.g., Rp-cGMPS; Fig. 1 *c*). The double-ligand cycle for HCN4 (Fig. 1 *c*) was utilized as a perturbation library for the chemical shift covariance analysis (CHESCA) (40,41). CHESCA takes advantage of the linear chemical shift-averaging typical of fast-exchanging equilibria, as in the case of the HCN4 CNBD $P_1 \Leftrightarrow P_2$ equilibrium, and is ideally suited to map residues subject to concerted transitions modulated by a targeted ligand library (40–43).

Our results for the HCN4 CNBD indicate that, although allostery is an essential driver of binding nonadditivity, the free energy of substituent coupling arises not only from the concerted inhibitory-to-active state $P_1 \Leftrightarrow P_2$ transition, but unexpectedly also from the nonadditivity of state-specific binding free energies. We show that active state-specific binding is highly nonadditive because of the presence of allosteric frustration (44,45), which was further probed through molecular dynamics (MD) simulations and mutations. On the contrary, full additivity was observed for the inhibitory state-specific binding, revealing that nonadditivity is surprisingly state-dependent. The state-dependency of the free energy of substituent coupling is a key determinant of partial agonism. Overall, our investigation illustrates how it is possible to elucidate by NMR unprecedented allosteric mechanisms underlying the coupling of substituent contributions to binding free energies. The identification of the key allosteric drivers of substituent nonadditivity is expected to facilitate the constructive exploitation of intersubstituent couplings in medicinal chemistry.

MATERIALS AND METHODS

Sample preparation

The HCN4 cAMP-binding domain constructs spanning residues 563–724 and 579–707 were prepared as described previously (15,46). The F689A mutants were created using a variation of the Quikchange protocol, as noted previously (46–48), and prepared similarly to the wild-type (wt) HCN4 samples. The concentration of HCN4 was determined using a Bradford assay and its purity was confirmed by SDS-PAGE. Cyclic AMP and GMP were purchased from Sigma Aldrich (ON, Canada), whereas all other cNMPs were purchased from Axxora (NY, USA). All cNMPs were prepared as 25 mM stock solutions.

Affinity measurements

Measurements of cNMP-binding affinities for HCN4 were achieved via competitive binding with the fluorescent cAMP analog, 8-NBD-cAMP, using an approach similar to the protocols described previously (49–51). The K_d of 8-NBD-cAMP for each HCN4 construct was initially determined via a titration in which the 8-NBD-cAMP concentration was fixed at 500 nM and the HCN4 construct was added at concentrations ranging from 0.1 to 50 μM. The HCN4 and 8-NBD-cAMP concentrations were then fixed at 5 μM and 500 nM, respectively, and cNMPs were added to outcompete 8-NBD-cAMP from HCN4. Fluorescence data were acquired with a BioTek Cytation Five-Plate Reader (Biotek, VT, USA) using Corning 96-well half-area plates (product no. 3881; Corning, NY, USA). The sample was excited at 485 nm and emission was recorded at 535 nm. Data was normalized relative to the fluorescence of 8-NBD-cAMP in the presence (max fluorescence) and absence (min fluorescence) of HCN4 and scaled according to the fraction of bound 8-NBD-cAMP (<*v*>) expected in the absence of competing ligand, determined from the equations described below. The K_d-values of the cNMPs were determined by fitting the competition curve with the following equation, as previously described by Wang (49):

$$\langle v \rangle = \frac{[PB]}{[B]_T} = \frac{2\sqrt{a^2 - 3b}\cos\left(\frac{\theta}{3}\right) - a}{3K_{8NBD} + \left(2\sqrt{a^2 - 3b}\cos\left(\frac{\theta}{3}\right) - a\right)}$$

where

$$a = K_{cNMP} + K_{8NBD} + [A]_T + [B]_T - [P]_T$$

$$b = K_{8NBD}\left([A]_T - [P]_T\right) + K_{cNMP}\left([B]_T - [P]_T\right) + K_{cNMP}K_{8NBD}$$

$$c = -K_{cNMP}K_{8NBD}[P]_T$$

$$\theta = arcos\frac{-2a^3 + 9ab - 27c}{2\sqrt{(a^2 - 3b)^3}}$$

$[A]_T$, $[B]_T$, and $[P]_T$ correspond to the total concentrations of the competing cNMP, 8-NBD-cAMP and HCN4, respectively, whereas K_{cNMP} and K_{8NBD} are the dissociation constants of the competing cNMP and the 8-NBD-cAMP ligands, respectively. [PB] represents the concentration of 8-NBD-cAMP bound to HCN4 and $<v>$ defines the fraction of bound 8-NBD-cAMP.

NMR spectroscopy

NMR data were acquired on a Bruker AV 700 spectrometer (Bruker, MA, USA) equipped with a 5-mm TCI cryoprobe. All experiments were acquired at 300 K. Gradient and sensitivity enhanced HSQC spectra were acquired on 100 μM samples of HCN4 constructs with $>$1 mM concentrations of cNMPs and 50 μM ^{15}N-acetyl glycine, for internal chemical shift referencing. Saturation of HCN4 was confirmed either by performing a full titration and reaching plateau or by acquiring spectra at three consecutive concentrations for which there were no significant chemical shift changes. The HSQC data were processed with NMRpipe, analyzed in Sparky and assigned via comparison with wt spectra or from chemical shift titrations. Chemical shift correlation plots were constructed as described previously (47,52), using the chemical shift difference between wt cAMP-bound and apo states as a reference (x axis) and the chemical shift difference between the perturbed state (cNMP-bound, mutant, etc.) and wt apo state for the y axis, except for the 579–707 construct. For this deletion construct, the y axis of the chemical shift correlation plot was determined from the difference between the perturbed state and the wt cAMP-bound state, as previously described (47). Only residues with an absolute cos (θ), as obtained from a CHESPA analysis, greater than 0.9 were plotted. In addition, all residues comprising the cAMP-binding pocket (i.e., BBR: 641–652; PBC: 658–672; Lid: 707–714) were removed because they sense nearest neighbor effects. The chemical shift projection analysis (CHESPA) was performed as described previously (15,46–48). The wt cAMP-bound and apo states were used as the reference vector for all analyses, whereas the perturbation vector was constructed from the difference between the perturbed state (cNMP-bound, mutant, etc.) and the wt apo state, unless otherwise stated. The cos (θ) value was only calculated for residues with a combined chemical shift difference greater than the cutoff of 0.025 ppm for the perturbation vector. Alternatively, the fractional shifts measured through the slopes of the chemical shift correlation plots are also obtained through the normalized PC1 components of the CHESCA singular value decomposition. The CHESCA and the chemical shift correlation analyses were performed as previously described (40,41), but the singular value decomposition analysis was performed using the apo chemical shifts as reference rather than those of Rp-cAMPS. This is because Rp-cAMPS is not a reverse agonist for HCN4.

The free ligand chemical shift data utilized to gauge intraligand covalent effects were acquired as follows. Each cNMP was prepared as a 5-mM sample in D_2O with 5 mM of TSP. For each sample, 1D ^{1}H, 1D ^{13}C, 1D DEPT, and 2D {^{1}H-^{13}C}-HSQC spectra were acquired. The 1D ^{1}H spectra were acquired with 32,768 complex points and a spectral width of 12 ppm centered at 4.7 ppm, whereas the 1D ^{13}C spectra were acquired with 65,536 complex points and a spectral width of 200 ppm centered at 100 ppm. The 1D ^{1}H spectra were acquired with 32 scans and 16 dummy scans, whereas the 1D ^{13}C spectra were acquired with 2000 scans and 32 dummy scans. The DEPT experiment was acquired with similar conditions to the 1D ^{13}C spectra except with 512 scans and a recycle delay of 1 s. The HSQC spectrum was acquired with 1000 and 128 complex points in the direct and indirect dimensions, respectively, eight scans, 32 dummy scans, and a recycle delay of 1.5 s.

MD simulations

MD simulations in explicit solvent were performed for the Rp-cAMPS-bound monomer of the intracellular region (IR) of human HCN4, which includes the CNBD. The total simulation time was 1.05 μs. The simulations were set up and executed following a protocol previously validated for the apo and cAMP-bound HCN4 IR (53).

Initial structure preparation protocol

The HCN4 IR construct spanning residues 521–717 of the HCN4 intracellular region was used for all MD simulations, as 717 is the last residue in the X-ray crystal structure. An initial cAMP-bound monomer structure was obtained from the x-ray crystal structure of the cAMP-bound IR (Protein Data Bank, PDB: 3OTF) by first deleting all water molecules from the structure and using SwissPDB Viewer to reconstruct partially missing side chains on the protein surface. The corresponding Rp-cAMPS-bound monomer structure was then obtained by editing the PDB text file, changing the equatorial exocyclic phosphate oxygen atom of the bound cAMP to a sulfur atom. Molecular structure topology and parameters data formatted for use with the CHARMM all-atom force field were generated for the Rp-cAMPS molecule using the online SwissParam software, and the topology and parameters data inserted into the respective parameter files for the CHARMM27 force field in preparation for subsequent MD simulation set-up.

MD simulation protocol

The MD simulations were performed in triplicate using the NAMD 2.9 software on the Shared Hierarchical Academic Research Computing Network. The CHARMM27 force field with CMAP correction, supplemented with the molecular structure topology and parameters data computed for the Rp-cAMPS molecule, was implemented. Simulation set-up and execution using the supplemented force field was performed following a protocol similar to that previously utilized for the apo and cAMP-bound HCN4 IR monomer simulations, resulting in a total simulation time of 1.05 μs.

Analysis of HCN4 IR structural dynamics

Structure similarity measures. To assess the propensities of the major HCN4 IR structural components for active- versus inactive-like structural arrangements, the simulations were analyzed through calculation of RMSD-based active-versus-inactive structure similarity measures (SMs) (53), where SM-values approaching 1 or -1 indicate protein conformations with fully active- or inactive-like structural arrangements, respectively. The distributions of SM-values for the HCN4 IR structures generated by the Rp-cAMPS-bound monomer simulations were computed following a protocol similar to that implemented previously (53), compiling the SM-values for all three replicate simulations into a single data set for examination, and using the previously-computed SM-value distributions for the apo and cAMP-bound monomer simulations as benchmarks for comparison (53).

Assessment of steric clashes

Potential energies of steric contact. To assess the suspected steric clash between the PBC and B-C structural elements in the presence of bound Rp-cAMPS, potential energies of steric contact between the PBC and B-C structural elements (i.e., residues 659–671 and 687–711 of HCN4, respectively), and between PBC residue L663 and B-helix residue F689, were computed for the HCN4 IR structures generated by the Rp-cAMPS-bound monomer simulations, with corresponding potential energies calculated from the cAMP-bound monomer simulations used as benchmarks for comparison. For each simulation, van der Waals (VDW) potential energies were computed using NAMD 2.9 with the CHARMM27 force field, implementing the same energy calculation parameters used in the simulations but with no nonbonded cutoff, and during each energy calculation, the portion(s) of the protein to be analyzed were specified using NAMD's Pair Interaction tool. VDW potential energies were calculated for each aforementioned pair of structural elements/residues, and for the separate structural elements/residues in each pair, and the potential energies of steric contact between the structural elements/residues in each pair were then computed from the VDW potential energies as follows: $PE_{steric;\ X\ vs.\ Y} = VDW_{X\ and\ Y\ together} - VDW_{X\ separate} - VDW_{Y\ separate}$, where "X" and "Y" are the two structural elements/residues in the pair, and the "VDW" terms are the calculated VDW potential energies obtained using NAMD. Boxplots were then constructed using Origin 9.1 (OriginLab Corporation), based on the data from the three replicates for each state.

RESULTS AND DISCUSSION

Allostery is a key driver of nonadditive substituent contributions to ligand binding in HCN4

The measurement of affinities through fluorescence competition for the double-ligand cycle in Fig. 1 *c* reveals that the A-to-G and Rp substitutions in cAMP cause losses of affinity by approximately one and two orders of magnitude, respectively, when implemented in isolation (Fig. 2, *a* and *b*; Table S1). However, when the A-to-G replacement is applied to the phosphorothioate Rp-cAMPS analog, it surprisingly leads to a gain of affinity (Fig. 2, *a* and *b*; Table S1). Using Eq. 2, the resulting γ_{Exp} nonadditivity factor is 19.6 ± 1.7 (Table S1), which is significantly above the thermal RT benchmark, pointing to significant positive cooperativity for the double-ligand cycle in Fig. 1 *c*.

To check to what extent the nonadditivity in the double-ligand cycle of Fig. 1 *c* arises from conformational exchange, we extended the measurement of the γ_{Exp} factor to an allosterically silenced mutant (i.e., HCN4 707X). In HCN4 707X, the inhibitory (P_1) versus active (P_2) transition is silenced by the removal of an indispensable driver of activation, i.e., the C-terminal lid. The removal of the lid locks HCN4 707X primarily in the P_1 state (Fig. S2, *a–f*). Hence, if the $P_1 \Leftrightarrow P_2$ conformational exchange is the key determinant of nonadditivity, we expect that the γ_{Exp} factor for the lidless mutant should approach unity. The measured affinities do indeed confirm that the γ_{Exp} factor observed for HCN4 707X is only 1.2 ± 0.1 (Fig. S2, *g* and *h*; Table S1), which is close to unity and well within the RT benchmark [e^{-1}, e] range, indicating negligible nonadditivity for the allosterically silenced HCN4 707X mutant.

The HCN4 707X results reveal that the dynamic inhibitory versus active conformational equilibrium of the HCN4 CNBD (i.e., the $P_1 \Leftrightarrow P_2$ exchange; Fig. S1 *b*) is an essential determinant of nonadditivity for the ligand

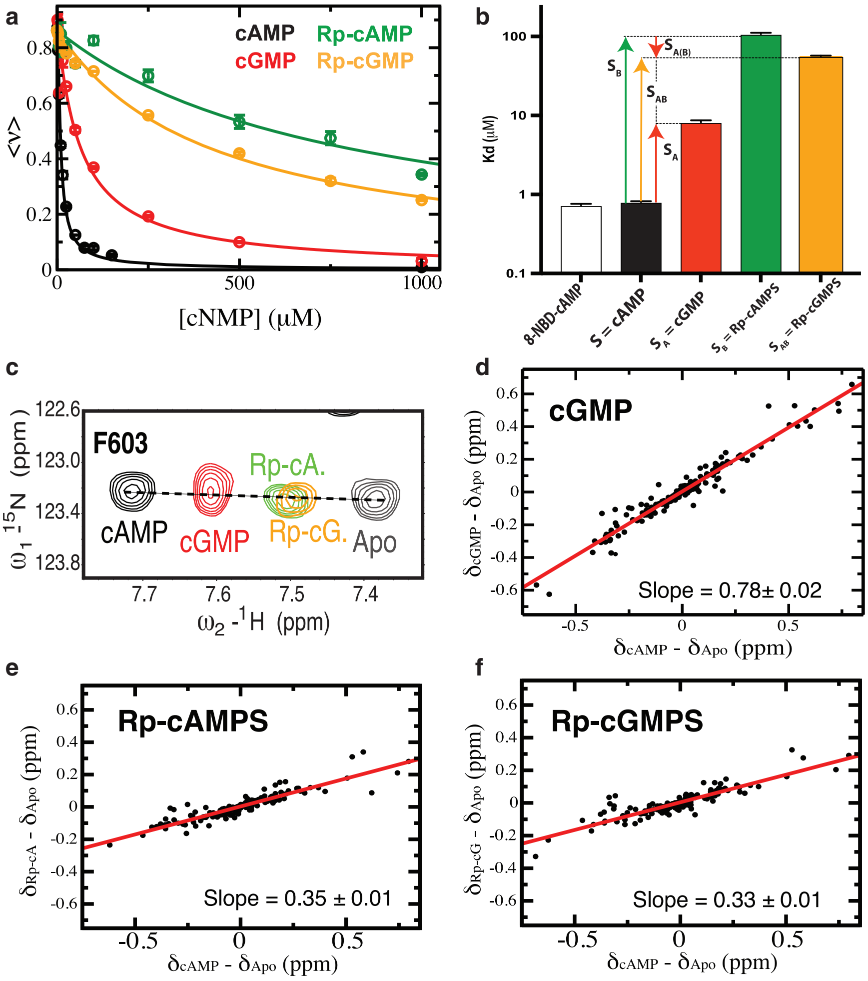

FIGURE 2 Nonadditivity in the Rp/G double-ligand cycle for the HCN4 CNBD. (*a*) Binding competition isotherms for cNMP analogs versus the fluorescent 8-NBD-cAMP ligand. The cAMP analogs are those in the nonadditivity cycle of Fig. 1 *c*. The Rp-cAMP/cGMP and Rp-cAMPS/cGMPS notations are used interchangeably in this paper. (*b*) K_d-values for the cAMP analogs in the previous panel, shown as a log scale bar plot. The K_d of 8-NBD-cAMP was measured by direct titration. The K_d-values are also reported in Table S1. Error bars were obtained from replicate measurements. The vertical arrows indicate the affinity changes caused by the A, B, A (B), and AB substitutions. The A (B) notation indicates that the A substitution occurs in the presence of B. (*c*) NH-HSQC spectral expansion of residue F603 in the HCN4 CNBD in the presence of saturating amounts of the cNMP analogs in the double-ligand cycle of Fig. 1 *c*. The F603 position in the HSQC spectrum reports primarily on the shifts in the fast-exchanging HCN4 CNBD autoinhibitory $P_1 \Leftrightarrow P_2$ equilibrium relative to the cAMP-bound and apo samples. (*d–f*) Chemical shift correlation plots for the cNMP analogs in (*c*). The slopes reflect the fractional activation relative to the cAMP-bound and apo HCN4 CNBD samples. Errors for the slopes were obtained from linear regressions. To see this figure in color, go online.

cycle of Fig. 1 *c*, ruling out significant contributions from intraligand through bond-covalent cross talk (e.g., inductive or electromeric effects). This conclusion is further supported by the absence of significant ^{1}H and ^{13}C chemical shift changes observed for the base upon introduction of the equatorial sulfur in Rp-cAMPS (Fig. S3). Hence, the near unity value of the γ_{Exp} measured for HCN4 707X and the chemical shift data (Figs. S2 and S3) consistently indicate that the free energy of coupling between the phosphate and base modifications (Fig. 1 *c*) arises primarily from noncovalent sources beyond the single-P$_1$ state, i.e., the P$_1$ ⇔ P$_2$ transition and/or contributions specific of the P$_2$ state.

A concerted P$_1$ ⇔ P$_2$ transition contributes to nonadditive binding but is insufficient alone to fully account for the observed nonadditivity

The contribution to the overall experimental nonadditivity factor γ_{Exp} arising uniquely from the P$_1$ ⇔ P$_2$ equilibrium is denoted here as γ_{12}. Because in the assessment of γ_{12} the transition between states 1 and 2 is assumed to be the sole source of nonadditivity, the binding to each state is expected to be additive, i.e., $K_{iAB}K_{iS} = K_{iA}K_{iB}$ with $i = 1$ or 2. In this case, the γ_{12} contribution can be estimated starting from the state populations in the P:S, P:S$_A$, and P:S$_B$ complexes (Fig. 1 *a*) using the theory of thermodynamic linkage (8,54) implemented through binding polynomials (55), as shown in Section S1:

$$\gamma_{12} = \frac{x_{1,A}x_{1,B}}{x_{1,S}} + \frac{x_{2,A}x_{2,B}}{x_{2,S}}, \tag{3}$$

where $x_{1,j}$ and $x_{2,j}$ are the fractions of states P$_1$ and P$_2$, respectively, in the macromolecule P saturated with the S$_j$ ligand in the cycle, i.e., the scaffold ligand S or the singly substituted ligands S$_A$ and S$_B$ (Figs. 1 *a* and S1 *b*). NMR spectroscopy is ideally suited to measure these state fractions.

If the exchange between conformations P$_1$ and P$_2$ is fast, as previously shown for the HCN4 CNBD (15), the relative populations of states P$_1$ and P$_2$ are measured directly from the NMR peak positions, by taking advantage of the fact that the observed chemical shifts are linear averages of the state-specific chemical shifts. For example, the NMR chemical shift changes for HCN4 residues sufficiently distant from the cAMP-binding site report primarily on the two-state inhibitory versus active equilibrium, e.g., F603 in the N3A shows that saturation with Rp-cAMPS or cGMP causes a linear shift away from cAMP and toward the apo position (Fig. 2 *c*). The fractional shifts reported by F603 are corroborated and quantified through more exhaustive chemical shift correlation analyses (Fig. 2, *d–f*; (52,56,57)). The slopes of the ($\delta_{Sj} - \delta_{Apo}$) versus ($\delta_{cAMP} - \delta_{Apo}$) plots in Fig. 2, *d–f* provide fractional activation shifts, denoted as $\langle X_j \rangle$, for P in the P:S$_j$ complexes of the double-ligand cycle in Fig. 1 (Table S1). The $\langle X_j \rangle$ values in Table S1 are then converted into state populations, $x_{1,j}$ and $x_{2,j}$, using the apo and cAMP-bound wt HNC4 CNBD samples as well as the inhibitory 707X mutant as references (Section S2). If the exchange between states P$_1$ and P$_2$ is slow or intermediate in the NMR chemical shift timescale, the state populations are reliably measured through chemical exchange saturation transfer or NMR dispersion experiments (Fig. S5; (58–60)).

In the case of the double-ligand cycle in Fig. 1 *c*, once the $x_{1,j}$ and $x_{2,j}$ values were determined using the fractional shifts in Fig. 2, *d* and *e*, the γ_{12} value was computed based on Eq. 3 to be 9.6 ± 0.7 (Fig. 3; Table S1). This result reveals that, although γ_{12} accounts for a significant fraction of the observed nonadditivity (~50%; Fig. 3; Table S1), the transition between states 1 and 2 alone is not sufficient to fully recapitulate the observed binding nonadditivity as quantified by γ_{Exp}. In addition, as explained in Section S3, the residual agonism quantified by the $\langle X_{AB} \rangle$ fractional activation observed for the doubly substituted ligand (Fig. 2 *f*; Table S1) cannot be explained by the P$_1$ ⇔ P$_2$ equilibrium alone with the assumption of additive state-specific binding (i.e., $K_{iAB}K_{iS} = K_{iA}K_{iB}$ with $i = 1$ or 2).

To solve these discrepancies, we hypothesized that the observed nonadditivity may arise not only from the P$_1$ ⇔ P$_2$ transition, but also from nonadditive state-specific binding. To gauge the latter contribution, we defined the state-specific nonadditivity factors, denoted as γ_1 and γ_2, in terms of state-specific association constants as opposed to the overall average association constants utilized in the definition of γ_{Exp}:

$$\gamma_i \equiv \frac{K_{iAB}K_{iS}}{K_{iA}K_{iB}} \text{ with } i = 1 \text{ or } 2, \tag{4}$$

where K_{ij} is the association constant for state *i* of the receptor macromolecule P and the S$_j$ ligand in the cycle (Fig. S1 *b*), i.e., S, S$_A$, S$_B$, or S$_{AB}$.

The P$_1$ ⇔ P$_2$ equilibrium together with nonadditive state-specific binding is sufficient to fully account for the observed nonadditivity

As shown in Section S4, the γ_1 and γ_2 nonadditivity factors are computed as:

$$\gamma_1 = \gamma_{Exp}\frac{x_{1,AB}\ x_{1,S}}{x_{1,A}\ x_{1,B}}, \tag{5}$$

$$\gamma_2 = \gamma_{Exp}\frac{x_{2,AB}\ x_{2,S}}{x_{2,A}\ x_{2,B}}, \tag{6}$$

where $x_{1,j}$ and $x_{2,j}$ are the fractions of states P$_1$ and P$_2$, respectively, in the macromolecule P saturated with one of the four S$_j$ ligands in the cycle, i.e., S, S$_A$, S$_B$, and S$_{AB}$ (Figs. 1 *c* and S1 *b*). Eqs. 5 and 6 show that the computation of state-specific nonadditivity factors requires not only the state populations of the P:S, P:S$_A$, and P:S$_B$ complexes, as

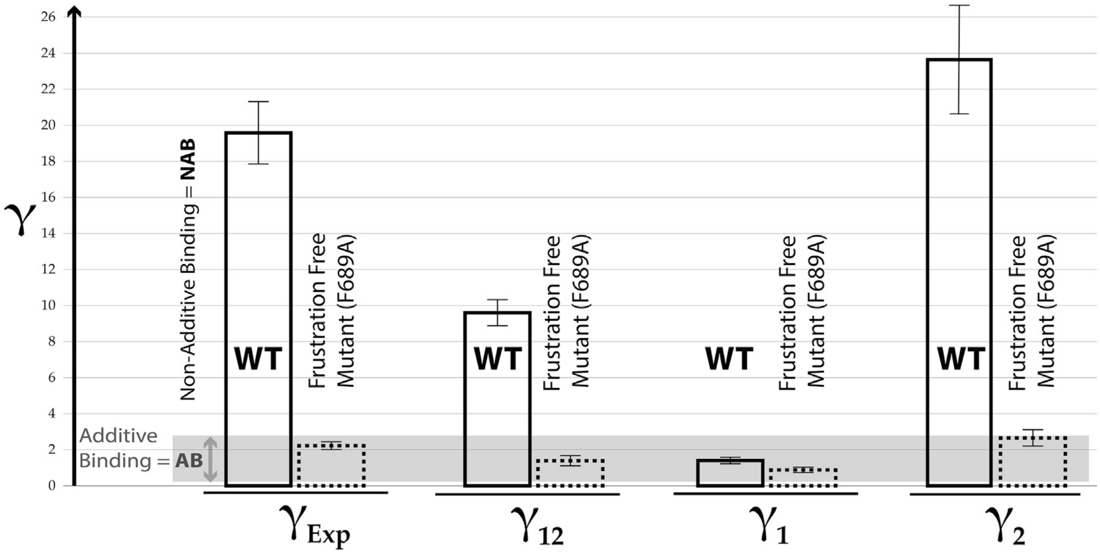

FIGURE 3 Dissection of the experimental nonadditivity factor (γ_{Exp}) into transition-specific (γ_{12}) and state-specific (γ_1 and γ_2) contributions. Shown are theγ-values for the Rp/G cycle of Fig. 1 *c* as applied to the HCN4 CNBD wt (*bars with solid lines*) and the frustration-free F689A mutant (*bars with dotted lines*). The gray region indicates γ-values that fall within the RT-benchmark window [e^{-1}, e], for which deviations from the additivity limit are assumed negligible. Error bars were obtained through error propagation.

in the case of γ_{12} (Eq. 3), but also the γ_{Exp} value and the state populations of the doubly substituted complex P:S$_{AB}$. As a result, the inclusion of the state-specific nonadditivity factors γ_1 and γ_2 ensures consistency with the observed nonadditivity factor (γ_{Exp}) as well as all fractional activations ($\langle X_j \rangle$), thereby resolving the discrepancy previously encountered when assuming that nonadditivity originates uniquely from the $P_1 \Leftrightarrow P_2$ equilibrium.

The γ_1 and γ_2 factors offer unique insight on additional mechanisms of intersubstituent allosteric coupling beyond the $P_1 \Leftrightarrow P_2$ transition, and they reveal how nonadditivity varies across different states. For example, the γ_1 and γ_2 factors computed for the Rp/G cycle (Fig. 1 *c*) using Eqs. 5 and 6 reveal that state-specific contributions to nonadditivity are highly variable. They arise primarily from conformation P_2, as indicated by a γ_1 value in the [e^{-1}, e] range and a significantly higher γ_2 ($\gamma_1 = 1.4 \pm 0.2$; $\gamma_2 = 23.6 \pm 3.0$; Fig. 3; Table S1). Notably, the computed γ_1 value for the wt HCN4 CNBD is in remarkably good agreement with the experimental nonadditivity factor measured for the lidless 707X mutant, which traps the inhibitory state P_1 ($\gamma_{Exp,707X} = 1.2 \pm 0.1$; Table S1). This agreement corroborates our computations and confirms the absence of significant nonadditivity for state P_1.

The additivity in conformer P_1 is consistent with the disengagement of the cNMP base from the lid in this state, as is typical of autoinhibitory conformations (Fig. 1 *d*). In marked contrast to γ_1, γ_2 significantly exceeds the RT-based threshold (Fig. 3; Table S1) and explains why the fractional activation observed for the CNBD bound to the doubly substituted Rp-cGMPS ligand is approximately one order of magnitude higher than expected based on the assumption of additivity for both the P_1 and P_2 states (0.33 ± 0.01 vs. 0.02 ± 0.01; Table S1). Hence, the nonadditivity of state P_2 (i.e., the active conformation) is a major driver of both the overall experimental nonadditivity (γ_{Exp}) and of the partial agonism observed for Rp-cGMPS. It is therefore critical to further investigate the determinants of γ_2.

Steric frustration is a major determinant of state-specific-binding nonadditivity (γ_2)

The high γ_2 value (23.6 ± 3.0; Fig. 3; Table S1) points to significant nonadditivity arising specifically from conformation P_2. Because additivity is observed for P_1 (Table S1) and a key P_1 versus P_2 difference is the engagement of the lid region in the latter state, we computed the free energy of coupling between the lid and the ligand substitutions, i.e., G and Rp (Fig. 1 *c*). For this purpose, we relied on the mutant/ligand cycle of Fig. S1 *c* and the affinities measured for the 707X mutant (Table S1). We found that the lid/G $\Delta G_{coupling}$ is positive ($\Delta G_{lid/G\ coupling}$ ~1.6 ± 0.1 kcal/mol; Table S2), confirming that the A-to-G replacement destabilizes the interactions between the lid and the base.

Interestingly, we observed an even larger positive value for the lid/Rp $\Delta G_{coupling}$ ($\Delta G_{lid/Rp\ coupling}$ ~2.4 ± 0.1 kcal/mol; Table S2), indicating that the introduction of the Rp modification in the cAMP phosphate interferes with the lid-base interactions. This result is remarkable because the nucleotide phosphate does not interact directly with the lid and suggests that, when Rp-cAMPS binds to the active conformation of HCN4 (i.e., state P_2, with a fully engaged lid; Fig. 1, *d* and *e*), it introduces a tension or strain, i.e., the complex of state P_2 with Rp-cAMPS is frustrated (44,45).

As a first step toward understanding why the P_2:Rp-cAMPS complex is frustrated, we reverted to MD simulations, which suggest that a key determinant of frustration is the steric hindrance between the side chains of F689 in the B-helix and L663 in the PBC (Section S5 and Fig. S6). To confirm this hypothesis and measure the extent of steric frustration arising from the F689 side chain, we engineered the frustration-silencing F689A mutation and measured the affinities of this mutant for the four ligands in the double-ligand cycle (Fig. S7 *a*; Table S1). The F689A mutation is anticipated to compensate for the steric hindrance caused by the replacement of the equatorial exocyclic oxygen atom with the bulkier sulfur atom in the Rp-cAMPS:P_2 complex, without significantly affecting changes in hydrogen-bond strength resulting from electronic effects, such as the oxygen versus sulfur electronegativity difference. As expected, the affinities of the Rp containing cNMPs (i.e., Rp-cAMPS and Rp-cGMPS) are dramatically increased in the frustration-silenced F689A mutant versus wild-type HCN4 (Fig. S7 *a*; Table S1), consistent with the enhanced stability of the F689A HCN4:Rp complex due to the removal of steric frustration induced by the F689 phenyl side chain.

Based on the affinities measured for F689A (Table S1) and the mutant-ligand thermodynamic cycle in Fig. S1 *c*, the free energy of coupling between the F689 side chain and the Rp substitution is estimated to be ~1.7 ± 0.1 kcal/mol (Table S2). This value is of the same order of magnitude as the Rp-cAMPS versus cAMP steric destabilization gauged through MD simulations (Fig. S6 *d*) and accounts for most of the frustration in the wt HCN4 CNBD arising from the recruitment of the lid in the presence of the Rp substitution, i.e., the ~2.4 kcal/mol lid/Rp-coupling free energy computed based on the 707X lidless mutant (Table S2). We conclude that the elimination of the F689/L663 steric clash (Fig. S6 *f*) in the F689A mutant enables a more effective recruitment of the lid region by the cNMP base, as is also confirmed by the marked increase in the fractional activations for both Rp-cNMPS (i.e., Rp-cAMPS and Rp-cGMPS) in going from the wild-type to the F689A HCN4 mutant (Fig. S7, *d* and *e*; Table S1). Overall, the F689A versus wt changes in affinities and fractional activation along the double mutant cycle (Fig. S7; Table S1) confirm the steric frustration between the F689 side chain and the Rp substituent predicted by the MD simulations (Fig. S6).

To test our hypothesis that the steric frustration arising from F689 is a key determinant of the elevated γ_2 value observed for the wt HCN4 CNBD, we measured γ_2 for the F689A mutant using the affinities and fractional activations of Fig. S7. As anticipated, the F689A versus wt changes in affinities and fractional activations (Table S1) translate into a reduction of γ_2 by approximately one order of magnitude to values that fall within the RT-benchmark region (Fig. 3; Table S1). This result points to negligible nonadditivity for state P_2 of the F689A mutant, confirming our hypothesis that the steric frustration of the P_2:Rp-cAMPS complex is a major determinant of γ_2. Such frustration is lost in the P_1:Rp-cAMPS complex because in the P_1 conformer, the B-C helices are disengaged and adopt an "out" orientation that releases the steric hindrance with F689. Hence, the steric frustration hypothesis explains not only the elevated value observed for γ_2 but also why γ_1 falls within the additive range in wt HCN4 (Fig. 3; Table S1).

Interestingly, the nonadditivity analysis of the F689A mutant reveals that this mutation reduces not only γ_2 but also γ_{12} to values within the additive range (Fig. 3; Table S1). This is an interesting observation because, unlike the allosterically silenced 707X mutant, the F689A mutant transitions from the P_1 to the P_2 state upon cAMP binding, and this transition occurs to an extent comparable to wt HCN4 ($<X_{cAMP,\mathrm{F689A}}> = 0.90 \pm 0.02$; Fig. S7 *c*; Table S1). This observation implies that the $P_1 \Leftrightarrow P_2$ transition alone is insufficient to generate nonadditive binding and other properties of such transition must be considered as well. For example, allosteric sites have been shown to locally violate the principle of minimal frustration (44,45). This notion suggests that the suppression of steric frustration by F689A may also disrupt the allosteric networks that ensure a concerted $P_1 \Leftrightarrow P_2$ transition, thus explaining why the γ_{12} value observed for the F689A mutant falls within the RT-benchmark level expected for near-additive binding.

The concerted nature of the $P_1 \Leftrightarrow P_2$ transition is a necessary determinant of the γ_{12} nonadditivity factor

To further support the hypothesis that the observed F689A versus wt γ_{12} reduction is caused by a loss of concertedness in the $P_1 \Leftrightarrow P_2$ transition because of compromised allosteric networks, we mapped such networks through comparative CHESCA analyses of the F689A versus wt HCN4 CNBD (Fig. 4). CHESCA is ideally suited to identify residue clusters subject to concerted transitions for fast-exchanging systems such as the HCN4 CNBD. Both the wt and F689A CHESCA analyses rely on the same perturbation library, which includes the four ligands that define the double-ligand cycle (Fig. 1 *c*) as well as the apo HCN4 CNBD.

The wt CHESCA-based allosteric map clearly shows that F689 serves as a major allosteric hub for the HCN4 CNBD, involved in multiple pairwise correlations with other residues in both the α- and β-subdomains (Fig. 4 *a*). As expected, F689 belongs to the main allosteric cluster of the HCN4 CNBD, as consistently indicated by both agglomerative clustering of the chemical shift correlation matrix (Fig. 4, *a* and *c*) and by singular value decomposition (Fig. S8, *a* and *b*). The allosteric role of the F689 phenyl group is further confirmed by the F689A mutant CHESCA, revealing a significant loss of correlations (Fig. 4, *b*, *d*, *g*, and *h*) relative to the wt HCN4 CNBD (Fig. 4, *a*, *c*, *e*, and *f*).

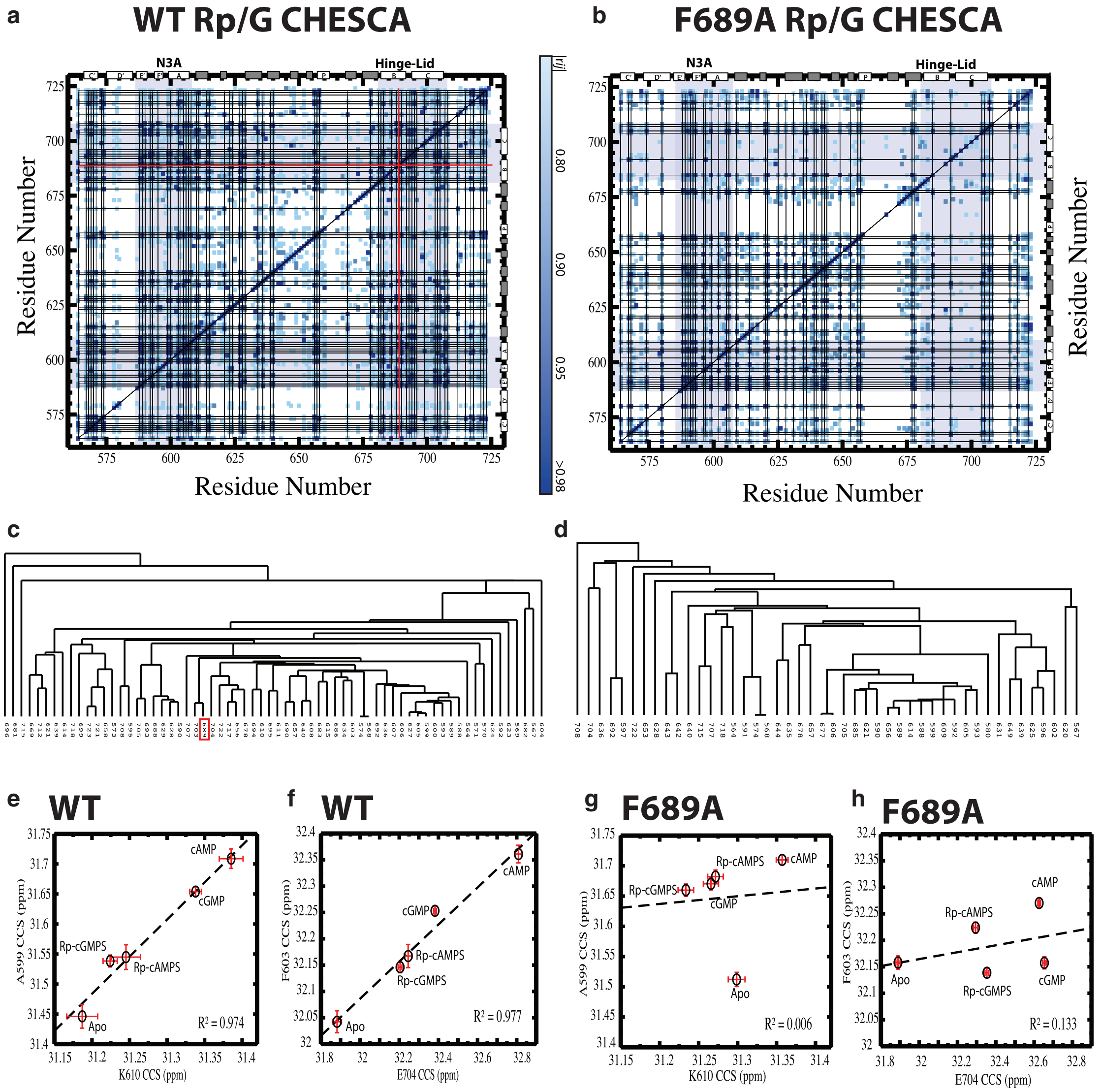

FIGURE 4 Chemical shift covariance analysis (CHESCA) of the HCN4 CNBD based on the Rp/G double-ligand cycle. (*a*) CHESCA correlation matrix for wt HCN4 (563–724) generated using the apo sample and the four cNMPs in the Rp/G cycle of Fig. 1 *c*. The secondary structure is shown as white (α-helices) and gray (β-strands) rectangles. The grid lines depict the single-linkage allosteric cluster of (*c*), whereas the red lines mark the position of F689. Shaded areas mark the N3A and hinge-lid helical regions. (*b*) As (*a*) but for the F689A HCN4 (563–724) mutant. (*c*) Dendrogram of the cluster obtained through single-linkage agglomerative clustering for the wt HCN4 CNBD. A Pearson's correlation coefficient cutoff ≥ 0.98 was utilized. F689 is highlighted by a red box. (*d*) As (*c*) but for the F689A HCN4 (563–724) mutant. (*e* and *f*) Representative pairwise interresidue combined chemical shift correlations for wt HCN4 (563–724). (*g* and *h*) Pairwise plots for the same residue pairs in (*e*) and (*f*) are shown but for F689A HCN4 (563–724), illustrating the decorrelation caused by the mutation, which perturbs the allosteric networks of wt HCN4. To see this figure in color, go online. Errors in the chemical shifts were assessed as previously described (40,41).

The CHESCA results (Fig. 4) clearly show that the F689 side chain is necessary to ensure a concerted allosteric $P_1 \Leftrightarrow P_2$ transition without significant sampling of transition intermediates, explaining why the γ_{12} value for the F689A mutant falls in the near-additivity range (Fig. 3; Table S1). Overall, the comparative CHESCA analyses of Fig. 4 reveal that the concertedness of the $P_1 \Leftrightarrow P_2$ transition is a key determinant of the γ_{12} contribution to binding nonadditivity. Furthermore, the one order of magnitude F689A versus wt reduction in the experimental γ_{Exp} to the RT-benchmark range (Fig. 3; Table S1) confirms the absence of other significant nonadditivity determinants (e.g., covalent ligand-based effects; Fig. 1 *b*) besides the concerted $P_1 \Leftrightarrow P_2$ allosteric transition and the frustration of state P_2, as quantified by γ_{12} and γ_2, respectively.

CONCLUSIONS

In conclusion, we have proposed an NMR-based approach to elucidate the allosteric mechanisms underlying nonadditive substituent contributions to ligand-binding. We have shown how, using NMR (Fig. S5), it is possible to

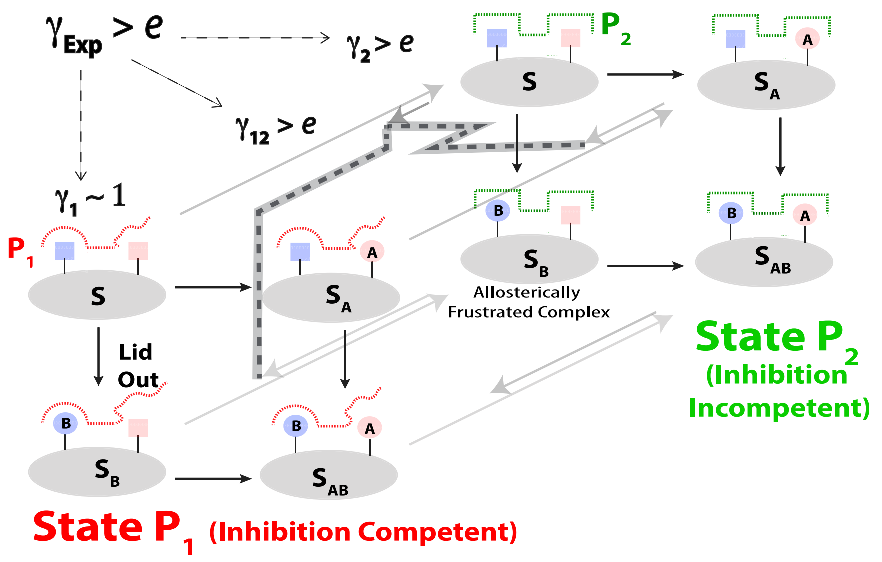

FIGURE 5 Allosteric mechanism of HCN4 nonadditivity for the Rp/G double-ligand cycle. The observed nonadditivity ($\gamma_{\mathrm{Exp}} > e$) for the HCN4 CNBD Rp/G double-ligand cycle is dissected in terms of three main contributions (γ_1, γ_2, and γ_{12}), which represent state- and transition-specific terms, respectively. The γ_1 factor is close to unity because the lid is disengaged from the base in state 1 (*wavy red dotted line*), resulting in negligible nonadditivity. The γ_{12} factor is $>e$ because both substituents drive the $P_1 \Leftrightarrow P_2$ two-state equilibrium in the same direction (*black dashed lines*) relative to the scaffold S, i.e., the unmodified cAMP ligand, giving rise to significant nonadditivity. The γ_2 factor is $>e$ primarily because of the allosteric frustration in the P_2:Rp-cAMPS complex. To see this figure in color, go online.

quantitatively dissect the experimental nonadditivity factor γ_{Exp} into transition- and state-specific contributions, i.e., γ_{12}, γ_1, and γ_2 (Fig. 3). The dissection of the experimental nonadditivity factor γ_{Exp} in terms of γ_{12}, γ_1, and γ_2 offers a means to analyze previously elusive mechanisms and driving forces underlying nonadditivity between substituents A and B (Fig. 5).

The γ_{12} value quantifies the contribution to nonadditivity arising uniquely from ligand-dependent modulations of the concerted $P_1 \Leftrightarrow P_2$ transition, and is primarily dictated by whether the two A and B substitutions shift the $P_1 \Leftrightarrow P_2$ equilibrium toward the same state (Fig. 5). The γ_{12} contribution to nonadditivity explains why ligand modifications that result in affinity losses when implemented in isolation, may lead to affinity gains when combined (Fig. 2, *a* and *b*). However, the γ_{12} term alone may not suffice to fully recapitulate the observed nonadditivity (i.e., γ_{Exp}) and the agonism of the doubly substituted ligand. It is, therefore, necessary to consider also the γ_1 and γ_2 descriptors of state-specific nonadditivity. They quantify the contributions to γ_{Exp} that cannot be captured solely by the two-state $P_1 \Leftrightarrow P_2$ transition and report on intersubstituent couplings specific of states P_1 and P_2, respectively (Fig. 5).

The application of the proposed NMR-based approach to the Rp/G double-ligand cycle for the prototypical allosteric HCN4 ion channel reveals that state-specific contributions to nonadditivity may arise from the release of steric frustration and may vary dramatically from state to state. For example, the γ_1 value specific of the inhibited state points to the absence of significant nonadditivity because of the disengagement of one of the critical binding sites in this state (i.e., the lid; Fig. 5). Unlike γ_1, the γ_2 value measured here indicates the presence of marked nonadditivity arising from the simultaneous engagement of both binding sites in the active state (i.e., the PBC and the lid), which results in steric frustration for the P_2:Rp-cAMPS complex (Fig. 5). The γ_1 versus γ_2 differential explains the partial agonism of the doubly substituted ligand. Furthermore, the molecular features underlying the γ_1 versus γ_2 differential (i.e., the L663/F689 residue pair linked to allosteric frustration) are highly conserved across CNBDs (37), suggesting that the state-specific nonadditivity observed for HCN4 may be a universal property of the ubiquitous cNMP-binding domain.

Overall, the proposed NMR-based analysis of nonadditive substituent contributions to binding free energies provides a widely applicable means to rationalize nonadditivity in mechanistic allosteric terms and constructively exploit it for the design of ligands with improved affinities and agonism. Ultimately, the inclusion of nonadditive effects in docking scoring functions and quantitative SAR models will further enhance these essential medicinal chemistry tools. Furthermore, we anticipate that the analyses and methods proposed here are generally applicable to allosteric receptors and signaling conformational switches, offering a new approach to analyze the molecular determinants that drive substituent nonadditivity.

SUPPORTING MATERIAL

Supporting Material can be found online at https://doi.org/10.1016/j.bpj.2020.07.038.

AUTHOR CONTRIBUTIONS

S.B., B.V., and G.M. designed research. S.B., K.V., B.V., J.A., and M.A. performed research. S.B., K.V., B.V., J.A., M.A., and G.M. analyzed data. B.V. and G.M. wrote the article.

ACKNOWLEDGMENTS

We thank Dr. F. Fogolari, Dr. S.S. Taylor, Dr. G. Veglia, Dr. F.W. Herberg, Dr. A. Moroni, Dr. W. Zagotta, Dr. Pietro Roversi, Romi Lifshitz, Alveena Ahmed, Nishi Parikh, and Rashik Ahmed for helpful discussions.

This work was supported by the Canadian Institutes of Health Research Grant 389522 (to G.M.) and the Natural Sciences and Engineering Research Council of Canada Grant RGPIN-2019-05990 (to G.M.).

REFERENCES

1. Klebe, G. 2015. Applying thermodynamic profiling in lead finding and optimization. *Nat. Rev. Drug Discov.* 14:95–110.
2. Tinberg, C. E., S. D. Khare, …, D. Baker. 2013. Computational design of ligand-binding proteins with high affinity and selectivity. *Nature.* 501:212–216.
3. Ye, L., C. Neale, …, R. S. Prosser. 2018. Mechanistic insights into allosteric regulation of the A_{2A} adenosine G protein-coupled receptor by physiological cations. *Nat. Commun.* 9:1372.
4. Warne, T., P. C. Edwards, …, C. G. Tate. 2019. Molecular basis for high-affinity agonist binding in GPCRs. *Science.* 364:775–778.
5. Sormanni, P., F. A. Aprile, and M. Vendruscolo. 2015. Rational design of antibodies targeting specific epitopes within intrinsically disordered proteins. *Proc. Natl. Acad. Sci. USA.* 112:9902–9907.
6. Dill, K. A. 1997. Additivity principles in biochemistry. *J. Biol. Chem.* 272:701–704.
7. Jencks, W. P. 1981. On the attribution and additivity of binding energies. *Proc. Natl. Acad. Sci. USA.* 78:4046–4050.
8. Di Cera, E., S. J. Gill, and J. Wyman. 1988. Binding capacity: cooperativity and buffering in biopolymers. *Proc. Natl. Acad. Sci. USA.* 85:449–452.
9. Baum, B., L. Muley, …, G. Klebe. 2010. Non-additivity of functional group contributions in protein-ligand binding: a comprehensive study by crystallography and isothermal titration calorimetry. *J. Mol. Biol.* 397:1042–1054.
10. Nasief, N. N., and D. Hangauer. 2015. Additivity or cooperativity: which model can predict the influence of simultaneous incorporation of two or more functionalities in a ligand molecule? *Eur. J. Med. Chem.* 90:897–915.
11. Kramer, C., J. E. Fuchs, and K. R. Liedl. 2015. Strong nonadditivity as a key structure-activity relationship feature: distinguishing structural changes from assay artifacts. *J. Chem. Inf. Model.* 55:483–494.
12. Reinhart, G. D. 1983. The determination of thermodynamic allosteric parameters of an enzyme undergoing steady-state turnover. *Arch. Biochem. Biophys.* 224:389–401.
13. Mesecar, A. D., and T. Nowak. 1997. Metal-ion-mediated allosteric triggering of yeast pyruvate kinase. 1. A multidimensional kinetic linked-function analysis. *Biochemistry.* 36:6792–6802.
14. Cherkasov, A., E. N. Muratov, …, A. Tropsha. 2014. QSAR modeling: where have you been? Where are you going to? *J. Med. Chem.* 57:4977–5010.
15. Akimoto, M., Z. Zhang, …, G. Melacini. 2014. A mechanism for the auto-inhibition of hyperpolarization-activated cyclic nucleotide-gated (HCN) channel opening and its relief by cAMP. *J. Biol. Chem.* 289:22205–22220.
16. Harzheim, D., K. H. Pfeiffer, …, R. Seifert. 2008. Cardiac pacemaker function of HCN4 channels in mice is confined to embryonic development and requires cyclic AMP. *EMBO J.* 27:692–703.
17. Lolicato, M., A. Bucchi, …, A. Moroni. 2014. Cyclic dinucleotides bind the C-linker of HCN4 to control channel cAMP responsiveness. *Nat. Chem. Biol.* 10:457–462.
18. Stathopulos, P. B., and M. Ikura. 2017. Store operated calcium entry: from concept to structural mechanisms. *Cell Calcium.* 63:3–7.
19. Doucet, N., P. Y. Savard, …, S. M. Gagné. 2007. NMR investigation of Tyr105 mutants in TEM-1 β-lactamase: dynamics are correlated with function. *J. Biol. Chem.* 282:21448–21459.
20. Carroll, M. J., R. V. Mauldin, …, A. L. Lee. 2012. Evidence for dynamics in proteins as a mechanism for ligand dissociation. *Nat. Chem. Biol.* 8:246–252.
21. Carroll, M. J., A. V. Gromova, …, A. L. Lee. 2011. Direct detection of structurally resolved dynamics in a multiconformation receptor-ligand complex. *J. Am. Chem. Soc.* 133:6422–6428.
22. Pagano, K., R. Torella, …, L. Ragona. 2012. Direct and allosteric inhibition of the FGF2/HSPGs/FGFR1 ternary complex formation by an antiangiogenic, thrombospondin-1-mimic small molecule. *PLoS One.* 7:e36990.
23. Tomaselli, S., K. Pagano, …, L. Ragona. 2015. Lipid binding protein response to a bile acid library: a combined NMR and statistical approach. *FEBS J.* 282:4094–4113.
24. Yu, C. H., N. Yang, …, O. Y. Dmitriev. 2017. The metal chaperone Atox1 regulates the activity of the human copper transporter ATP7B by modulating domain dynamics. *J. Biol. Chem.* 292:18169–18177.
25. Fayos, R., G. Melacini, …, P. A. Jennings. 2003. Induction of flexibility through protein-protein interactions. *J. Biol. Chem.* 278:18581–18587.
26. McNicholl, E. T., R. Das, …, G. Melacini. 2010. Communication between tandem cAMP binding domains in the regulatory subunit of protein kinase A-Ialpha as revealed by domain-silencing mutations. *J. Biol. Chem.* 285:15523–15537.
27. Byun, J. A., K. Van, …, G. Melacini. 2020. Mechanism of allosteric inhibition in the Plasmodium falciparum cGMP-dependent protein kinase. *J. Biol. Chem.* 295:8480–8491.
28. Walker, C., Y. Wang, …, G. Veglia. 2019. Cushing's syndrome driver mutation disrupts protein kinase A allosteric network, altering both regulation and substrate specificity. *Sci. Adv.* 5:eaaw9298.
29. Byun, J. A., M. Akimoto, …, S. S. Taylor. 2020. Allosteric pluripotency as revealed by protein kinase A. *Sci. Adv.* 6:eabb1250.
30. Wang, Y., M. v S, …, G. Veglia. 2019. Globally correlated conformational entropy underlies positive and negative cooperativity in a kinase's enzymatic cycle. *Nat. Commun.* 10:799.
31. De Simone, A., F. A. Aprile, …, M. Vendruscolo. 2015. Structure of a low-population intermediate state in the release of an enzyme product. *eLife.* 4:e02777.
32. Wodak, S. J., E. Paci, …, T. McLeish. 2019. Allostery in its many disguises: from theory to applications. *Structure.* 27:566–578.
33. Meng, W., E. M. Clerico, …, L. M. Gierasch. 2018. Allosteric landscapes of eukaryotic cytoplasmic Hsp70s are shaped by evolutionary tuning of key interfaces. *Proc. Natl. Acad. Sci. USA.* 115:11970–11975.
34. Kumar, G. S., M. W. Clarkson, …, W. Peti. 2018. Dynamic activation and regulation of the mitogen-activated protein kinase p38. *Proc. Natl. Acad. Sci. USA.* 115:4655–4660.
35. Tzeng, S.-R., and C. G. Kalodimos. 2012. Protein activity regulation by conformational entropy. *Nature.* 488:236–240.
36. Long, D., and R. Brüschweiler. 2011. Atomistic kinetic model for population shift and allostery in biomolecules. *J. Am. Chem. Soc.* 133:18999–19005.
37. Berman, H. M., L. F. Ten Eyck, …, S. S. Taylor. 2005. The cAMP binding domain : An ancient signaling module. *Proc. Natl. Acad. Sci. USA.* 102:4–9.
38. Xu, X., Z. V. Vysotskaya, …, L. Zhou. 2010. Structural basis for the cAMP-dependent gating in the human HCN4 channel. *J. Biol. Chem.* 285:37082–37091.
39. Akimoto, M., B. Vanschouwen, and G. Melacini. 2018. The structure of the apo cAMP-binding domain of HCN4 - a stepping stone toward understanding the cAMP-dependent modulation of the hyperpolarization-activated cyclic-nucleotide-gated ion channels. *FEBS J.* 285:2182–2192.

40. Boulton, S., R. Selvaratnam, …, G. Melacini. 2018. Implementation of the NMR CHEmical shift covariance analysis (CHESCA): a chemical biologist's approach to allostery. *Methods Mol. Biol.* 1688:391–405.
41. Selvaratnam, R., S. Chowdhury, …, G. Melacini. 2011. Mapping allostery through the covariance analysis of NMR chemical shifts. *Proc. Natl. Acad. Sci. USA.* 108:6133–6138.
42. Selvaratnam, R., M. T. Mazhab-Jafari, …, G. Melacini. 2012. The autoinhibitory role of the EPAC hinge helix as mapped by NMR. *PLoS One.* 7:e48707.
43. Chen, H., W. M. Marsiglia, …, M. Mohammadi. 2017. Elucidation of a four-site allosteric network in fibroblast growth factor receptor tyrosine kinases. *eLife.* 6:e21137.
44. Ferreiro, D. U., E. A. Komives, and P. G. Wolynes. 2014. Frustration in biomolecules. *Q. Rev. Biophys.* 47:285–363.
45. Ferreiro, D. U., E. A. Komives, and P. G. Wolynes. 2018. Frustration, function and folding. *Curr. Opin. Struct. Biol.* 48:68–73.
46. Boulton, S., M. Akimoto, …, G. Melacini. 2017. Free energy landscape remodeling of the cardiac pacemaker channel explains the molecular basis of familial sinus bradycardia. *J. Biol. Chem.* 292:6414–6428.
47. Moleschi, K. J., M. Akimoto, and G. Melacini. 2015. Measurement of state-specific association constants in allosteric sensors through molecular stapling and NMR. *J. Am. Chem. Soc.* 137:10777–10785.
48. Boulton, S., R. Selvaratnam, …, G. Melacini. 2018. Mechanism of selective enzyme inhibition through uncompetitive regulation of an allosteric agonist. *J. Am. Chem. Soc.* 140:9624–9637.
49. Wang, Z.-X. 1995. An exact mathematical expression for describing competitive binding of two different ligands to a protein molecule. *FEBS Lett.* 360:111–114.
50. Zhu, Y., H. Chen, …, X. Cheng. 2015. Biochemical and pharmacological characterizations of ESI-09 based EPAC inhibitors: defining the ESI-09 "therapeutic window". *Sci. Rep.* 5:9344.
51. Shao, H., H. Mohamed, …, G. Melacini. 2020. Mechanism of action of an EPAC1-selective competitive partial agonist. *J. Med. Chem.* 63:4762–4775.
52. Lorieau, J. L., J. M. Louis, …, A. Bax. 2012. pH-triggered, activated-state conformations of the influenza hemagglutinin fusion peptide revealed by NMR. *Proc. Natl. Acad. Sci. USA.* 109:19994–19999.
53. VanSchouwen, B., M. Akimoto, …, G. Melacini. 2015. Role of dynamics in the autoinhibition and activation of the hyperpolarization-activated cyclic nucleotide-modulated (HCN) ion channels. *J. Biol. Chem.* 290:17642–17654.
54. Weber, G. 1992. Protein interactions. Chapman and Hall, London, UK.
55. Dill, K. A., and S. Bromberg. 2003. Molecular Driving Forces: Statistical Thermodynamics in Chemistry and Biology. Garland Science, New York.
56. Selvaratnam, R., B. VanSchouwen, …, G. Melacini. 2012. The projection analysis of NMR chemical shifts reveals extended EPAC autoinhibition determinants. *Biophys. J.* 102:630–639.
57. Cembran, A., J. Kim, …, G. Veglia. 2014. NMR mapping of protein conformational landscapes using coordinated behavior of chemical shifts upon ligand binding. *Phys. Chem. Chem. Phys.* 16:6508–6518.
58. Vallurupalli, P., A. Sekhar, …, L. E. Kay. 2017. Probing conformational dynamics in biomolecules via chemical exchange saturation transfer: a primer. *J. Biomol. NMR.* 67:243–271.
59. Loria, J. P., M. Rance, and A. G. Palmer. 1999. A relaxation-compensated Carr−Purcell−Meiboom−Gill sequence for characterizing chemical exchange by NMR spectroscopy. *J. Am. Chem. Soc.* 121:2331–2332.
60. Vallurupalli, P., D. F. Hansen, and L. E. Kay. 2008. Structures of invisible, excited protein states by relaxation dispersion NMR spectroscopy. *Proc. Natl. Acad. Sci. USA.* 105:11766–11771.

Biophysical Journal, Volume *119*

Supplemental Information

Allosteric Mechanisms of Nonadditive Substituent Contributions to Protein-Ligand Binding

Stephen Boulton, Katherine Van, Bryan VanSchouwen, Jerry Augustine, Madoka Akimoto, and Giuseppe Melacini

Section 1. Calculation of the Transition-Specific Non-Additivity Factor γ_{12}. In the case where the apo protein P samples an equilibrium between two conformations (P_1 and P_2) with equilibrium constant: $\alpha \equiv x_{1,Apo}/x_{2,Apo}$, the binding polynomials (Q) for the P:S, P:S_A and P:S_B complexes are:

$$Q_S = \alpha\,(1 + K_{1S}[S]) + (1 + K_{2S}[S])$$

$$Q_{SA} = \alpha\,(1 + K_{1A}[S_A]) + (1 + K_{2A}[S_A])$$

$$Q_{SB} = \alpha\,(1 + K_{1B}[S_B]) + (1 + K_{2B}[S_B])$$

$$Q_{SAB} = \alpha\,(1 + K_{1AB}[S_{AB}]) + (1 + K_{2AB}[S_{AB}])$$

where K_{1j} and K_{2j} are the state-specific association constants for ligands j = S, S_A, S_B or S_{AB}, respectively. Based on these binding polynomials, the fractional saturation of P with respect to each ligand S_j is computed as (1):

$$< \upsilon_{S_j} > = \frac{\partial lnQ_{S_j}}{\partial \ln[S_j]}$$

which leads to:

$$< \upsilon_{S_j} > = \bar{K}_{S_j}[S_j] / (1 + \bar{K}_{S_j}[S_j])$$

where the $\bar{K}_{S_j}$ values are the averages of the respective state-specific association constants K_{1j} and K_{2j}, weighted according to the apo protein state populations: $\bar{K}_{S_j} = x_{1,Apo}\,K_{1j} + x_{2,Apo}\,K_{2j}$. Specifically, the association constants for the binding of S, S_A, S_B and S_{AB} to P are then:

$$\bar{K}_S = (\alpha\,K_{1S} + K_{2S}) / (\alpha + 1)$$

$$\bar{K}_A = (\alpha\,K_{1A} + K_{2A}) / (\alpha + 1)$$

$$\bar{K}_B = (\alpha\,K_{1B} + K_{2B}) / (\alpha + 1)$$

$$\bar{K}_{AB} = (\alpha\,K_{1AB} + K_{2AB}) / (\alpha + 1)$$

Therefore, γ for a dynamic protein receptor P subject to a two-state equilibrium, as defined by equation (2), becomes:

$$\gamma = \frac{\bar{K}_{AB}\,\bar{K}_S}{\bar{K}_A\,\bar{K}_B} = \frac{(\alpha\,K_{1AB} + K_{2AB})(\alpha\,K_{1S} + K_{2S})}{(\alpha\,K_{1A} + K_{2A})(\alpha\,K_{1B} + K_{2B})}$$

If the only source of non-additivity is the $P_1 \Leftrightarrow P_2$ equilibrium and additivity is assumed for the binding free energy contributions within each state (*i.e.* $K_{iAB} = K_{iA}\,K_{iB} / K_{iS}$ with i = 1 or 2), then:

$$\gamma_{12} = \frac{\left(\alpha \frac{K_{1A}\,K_{1B}}{K_{1S}} + \frac{K_{2A}\,K_{2B}}{K_{2S}}\right)(\alpha\,K_{1S} + K_{2S})}{(\alpha\,K_{1A} + K_{2A})(\alpha\,K_{1B} + K_{2B})}$$

If we define: $\sigma_j \equiv K_{1j}/K_{2j}$, then: $\gamma_{12} = \frac{(\alpha\,\sigma_A\,\alpha\,\sigma_B + \alpha\,\sigma_S)(\alpha\,\sigma_S + 1)}{(\alpha\,\sigma_A + 1)(\alpha\,\sigma_B + 1)(\alpha\,\sigma_S)}$

Considering that at ligand saturation: $\alpha_j = \alpha\, \sigma_j$ with $\alpha_j = x_{1,j}/x_{2,j}$ then:

$$\gamma_{12} = \frac{x_{1,A}x_{1,B}}{x_{1,S}} + \frac{x_{2,A}x_{2,B}}{x_{2,S}} \qquad (3).$$

Section 2. Conversion of Chemical-Shift Based Fractional Activations into State Populations. The slopes of the NMR chemical shift (δ) correlation plots in Fig. 2d-f provide directly the fractional activation ($< X_j >$) relative to the apo and the ligand S-saturated proteins, utilized as reference samples:

$$< X_j > = \left(\delta_j - \delta_{Apo}\right) / \left(\delta_S - \delta_{Apo}\right)$$

where the subscripts *S* and *j* denote the sample saturated with ligand S or S_j, respectively. This equation can be rewritten by considering that for a single residue in the macromolecule P saturated with ligand S_j and subject to a fast exchanging two-state equilibrium between states 1 and 2 (*i.e.* the 1 ⇔ 2 exchange), the observed chemical shift is a linear population-weighted average:

$$\delta_j = \delta_1 x_{1,j} + \delta_2 x_{2,j} \quad \text{or} \quad \delta_j = \delta_1 + (\delta_2 - \delta_1) x_{2,j}$$

where δ_j, δ_1 and δ_2 are the observed, state 1 and state 2 chemical shifts, respectively, for the selected residue under consideration. Hence, the equation for $< X_j >$ can be rewritten as:

$$< X_j > = \left(x_{2,j} - x_{2,Apo}\right) / \left(x_{2,S} - x_{2,Apo}\right)$$

or:

$$x_{2,j} = < X_j > \left(x_{2,S} - x_{2,Apo}\right) + x_{2,Apo}$$

where *j* denotes the ligand $S_j = S_A$, S_B or S_{AB}. This equation provides the state populations of the sample saturated with S_j starting from the relative fractional activation ($< X_j >$) and the state populations of the two reference samples, apo and *S, i.e.* $x_{2,\mathrm{Apo}}$ and $x_{2,\mathrm{S}}$. The latter is obtained from the former using the K_s and K_{1s} values, *e.g.* the affinities of ligand S for the wt protein and for state 1, as follows. The $\overline{K}_S = (\alpha K_{1S} + K_{2S}) / (\alpha + 1)$ equation derived above can be re-written as:

$$\overline{K}_S = K_{1S} x_{1,Apo} + K_{2S} \left(1 - x_{1,Apo}\right)$$

The second addendum in this equation can be recast as follows, considering that: $\alpha_S = \alpha\, \sigma_S$, where $\alpha \equiv x_{1,Apo}/x_{2,Apo}$ and $\sigma_S \equiv K_{1S}/K_{2S}$. So:

$$\frac{x_{1,S}}{(1 - x_{1,S})} = \frac{x_{1,Apo}}{(1 - x_{1,Apo})} \frac{K_{1S}}{K_{2S}}$$

or:

$$K_{2S} \left(1 - x_{1,Apo}\right) = \frac{(1 - x_{1,S})}{x_{1,S}} x_{1,Apo} K_{1S}$$

So:

$$\overline{K}_S = K_{1S} x_{1,Apo} + \frac{(1 - x_{1,S})}{x_{1,S}} x_{1,Apo} K_{1S}$$

or:

$$x_{1,S} = x_{1,Apo}\,\beta \quad \text{(S1)}, \quad \text{where:} \quad \beta \equiv \frac{K_{1S}}{K_S} \quad \text{(S2)}$$

These equations provide a means to recast the experimental relative fractional activations ($< X_j >$) into the populations of conformations P_1 and P_2 for the protein:ligand complexes defining the non-additivity cycle (*i.e.* $x_{1,j}$ and $x_{2,j}$ values with j = S, S_A, S_B and S_{AB}):

$$x_{1,j} = x_{1,Apo}[< X_j > (\beta - 1) + 1] \qquad \text{where:} \quad \beta \equiv \frac{K_{1S}}{K_S} \qquad \text{(S3)}$$

Since: $x_{2,j} = 1 - x_{1,j}$, equation S3 provides the state populations in the P:S_j complex starting from the apo populations and the association constants K_s and K_{1s}, which are experimentally accessible. The state-specific affinity K_{1s} is measured, as previously explained (2), by relying on a mutant ‘trapping’ the inactive state and the equation:

$$K_{1S} = K_{S,Mt}\,\frac{x_{1,S,Mt}}{x_{1,Apo,Mt}}$$

where the subscript *Mt* refers to measurements for the inactive state-trapping mutant (*e.g.* the lidless 707X truncation mutant in the case of HCN4).

Once the molar fractions are available through equation (S3), the transition-specific γ_{12} and the state-specific γ_1 and γ_2 are computed through equations (3), (5) and (6). For example:

$$\gamma_1 = \gamma_{Exp}\,\frac{[<X_{AB}>(\beta-1)+1]\;[<X_S>(\beta-1)+1]}{[<X_A>(\beta-1)+1]\;[<X_B>(\beta-1)+1]}$$

$$\gamma_2 = \gamma_{Exp}\,\frac{[1-x_{1,Apo}-x_{1,Apo}<X_{AB}>(\beta-1)]\;[1-x_{1,Apo}-x_{1,Apo}<X_S>(\beta-1)]}{[1-x_{1,Apo}-x_{1,Apo}<X_A>(\beta-1)]\;[1-x_{1,Apo}-x_{1,Apo}<X_B>(\beta-1)]}$$

or, since S is the reference state in the measurement of the fractional activations (*i.e.* $< X_S > \equiv 1$):

$$\gamma_1 = \gamma_{Exp}\,\frac{[<X_{AB}>(\beta-1)+1]\,\beta}{[<X_A>(\beta-1)+1]\;[<X_B>(\beta-1)+1]} \qquad \text{(S4)}$$

$$\gamma_2 = \gamma_{Exp}\,\frac{[1-x_{1,Apo}-x_{1,Apo}<X_{AB}>(\beta-1)]\;[1-\beta x_{1,Apo}]}{[1-x_{1,Apo}-x_{1,Apo}<X_A>(\beta-1)]\;[1-x_{1,Apo}-x_{1,Apo}<X_B>(\beta-1)]} \qquad \text{(S5)}$$

Based on these equations, γ_1 and γ_2 are calculated directly from the average fractional activations, γ_{Exp} and $K_{d,1S}$. Hence, no prior knowledge of $x_{1,Apo}$ is required for γ_1, but an estimation of $x_{1,Apo}$ is necessary for γ_2. Although $x_{1,Apo}$ is estimated to be > 0.9 (2), simulations show that the dependence of γ_2 on $x_{1,Apo}$ is not steep and largely within experimental error (Fig. S4). Similar considerations apply to the dependence of γ_{12} on $x_{1,Apo}$ (Fig. S4). Therefore, very approximate estimations of $x_{1,Apo}$ are likely to be sufficient for this purpose.

Section 3. P_1 ⇔ P_2 Equilibrium in P:S_{AB} in the Presence of State-Specific Additivity. The position of the auto-inhibitory equilibrium for P in the presence of saturating amounts of the S_{AB} ligand is defined by:

$\alpha_{AB} = x_{1,AB}/x_{2,AB} = \alpha\,\sigma_{AB}$ with $\sigma_{AB} \equiv K_{1AB}/K_{2AB}$

If we assume that other sources of non-additivity besides the dynamic equilibrium between states P_1 and P_2 are negligible, such that for each conformation (*i.e.* P_1 or P_2) the state-specific binding free energies are additive (*i.e.* $K_{iAB} = K_{iA} K_{iB} / K_{iS}$ with $i = 1$ or 2), then:

$$\alpha_{AB.12} = \alpha \, K_{1A} K_{1B} K_{2S} / (K_{2A} K_{2B} K_{1S})$$

where the 12 subscript denotes that the equilibrium constant was computed only based on the transition between states 1 and 2.

Considering that: $\alpha_j = \alpha \, \sigma_j$ with $\sigma_j \equiv K_{1j}/K_{2j}$, with the subscript j denoting ligand S_j, *i.e.* S, S_A or S_B, then:

$$\alpha_{AB,12} = \frac{\alpha_A \, \alpha_B}{\alpha_S}$$

Once $\alpha_{AB,12}$ is computed, the resulting $x_{1,AB}$ and $x_{2,AB}$ values are translated into fractional activations ($< X_{AB,12} >$) as explained in the previous section (Table S1). For example, for the double-ligand cycle of Fig. 1c, the pure $P_1 \Leftrightarrow P_2$ equilibrium predicts a marginal fractional activation for the doubly-substituted ligand of 0.02 ± 0.01 (Table S1), which is significantly lower than the observed value of 0.33 ± 0.01 (Fig. 2f; Table S1).

Section 4. Computation of State-Specific Non-Additivity Constants γ_1 and γ_2. Based on the definition of state-specific non-additivity constants:

$$\gamma_i \equiv \frac{K_{iAB} K_{iS}}{K_{iA} K_{iB}} \qquad \text{with } i = 1 \text{ or } 2 \quad (4)$$

Considering that, similarly to equations S1 and S2: $x_{1,S_j} = x_{1,Apo} \frac{K_{1S_j}}{K_{S_j}}$

equation (4) becomes:

$$\gamma_1 = \gamma_{Exp} \frac{x_{1,AB} \, x_{1,S}}{x_{1,A} \, x_{1,B}} \qquad (5)$$

Proceeding similarly for state 2, we obtain: $\gamma_2 = \gamma_{Exp} \frac{x_{2,AB} \, x_{2,S}}{x_{2,A} \, x_{2,B}}$ (6).

Section 5. MD Simulations of the HCN4 CNBD:Rp-cAMPS Complex. Three MD trajectories of 350 ns each were generated for the HCN4 CNBD:Rp-cAMPS complex. The resulting similarity indexes computed based on the MD trajectories (3) indicate that in the P_2:Rp-cAMPS complex the B-C helices largely preserve the 'in' topology typical of the cAMP-bound HCN4, but the PBC shifts towards the 'out' orientation to an extent comparable to apo HCN4 (Fig. S6a,b). The apo-like 'out' orientation of the PBC is consistent with the presence of the bulky equatorial sulfur atom of Rp-cAMPS (S *vs.* O van der Waals radius and P-S *vs.* P-O bond length increments of ~0.3 Å and ~0.4 Å, respectively (4), while the adenine base of Rp-cAMPS recruits the lid and the rest of the α-subdomain in conformation P_2 (Fig. S6e-g). The simultaneous presence of the α-subdomain in state 2 and the β-subdomain PBC in state 1 in the P_2: Rp-cAMPS complex suggests a steric clash between the sidechains of F689 in the B-helix and L663 of the PBC (Fig. S6f). The steric hindrance between the B-C and PBC helices, and specifically between residues F689 and L663, is also confirmed by the net increase in the Van der Waals potential energy between these structural elements in the HCN4 CNBD:Rp-cAMPS *vs.* CNBD:cAMP complexes (Fig. S6c,d). Overall, the MD simulations support the hypothesis that in the P_2:Rp-cAMPS complex, F689 in the B-helix sterically clashes against L663 in the PBC.

Supplementary Figures

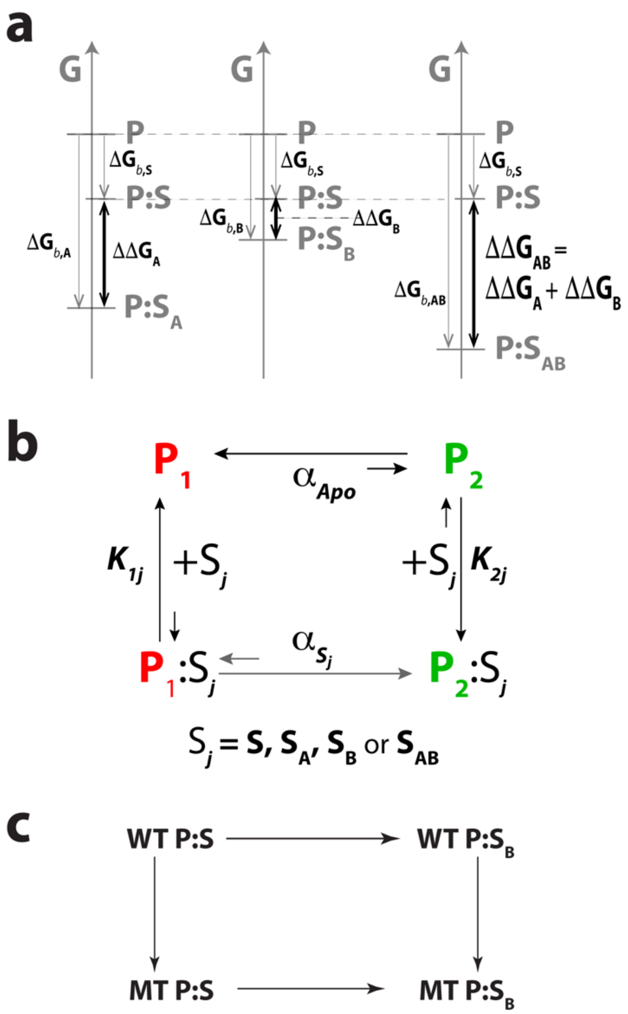

Figure S1. (a, b) *Double-Ligand Cycle Thermodynamics.* (a) Dissection of the free energy of binding for the double-substituted ligand S_{AB} in terms of substituent-specific contributions, when binding additivity applies. $\Delta G_{b,j}$ denotes the free energy of binding of ligand "*j*" to protein P. (b) Four-state thermodynamic cycles arising from the coupling between the $P_1 \Leftrightarrow P_2$ conformational equilibrium and the ligand binding equilibrium. The ligand S_j represents each of the four ligands in a double-ligand cycle (Fig. 1a). **(c)** *Thermodynamic Cycle for the Coupling between a Mutated Side-Chain and a Ligand Modification.* MT denotes a mutant, *e.g.* 707X or F689A, while S is the scaffold ligand and S_B a substituted ligand. For example in Fig. 1c, S = cAMP, S_B = Rp-cAMPS and P is the protein receptor, HCN4. This cycle enables the computation of mutant-ligand substituent coupling free energies as -RT ln ($K_{d,WT,cA}\, K_{d,MT,cA'} / K_{d,MT,cA}\, K_{d,WT,cA'}$).

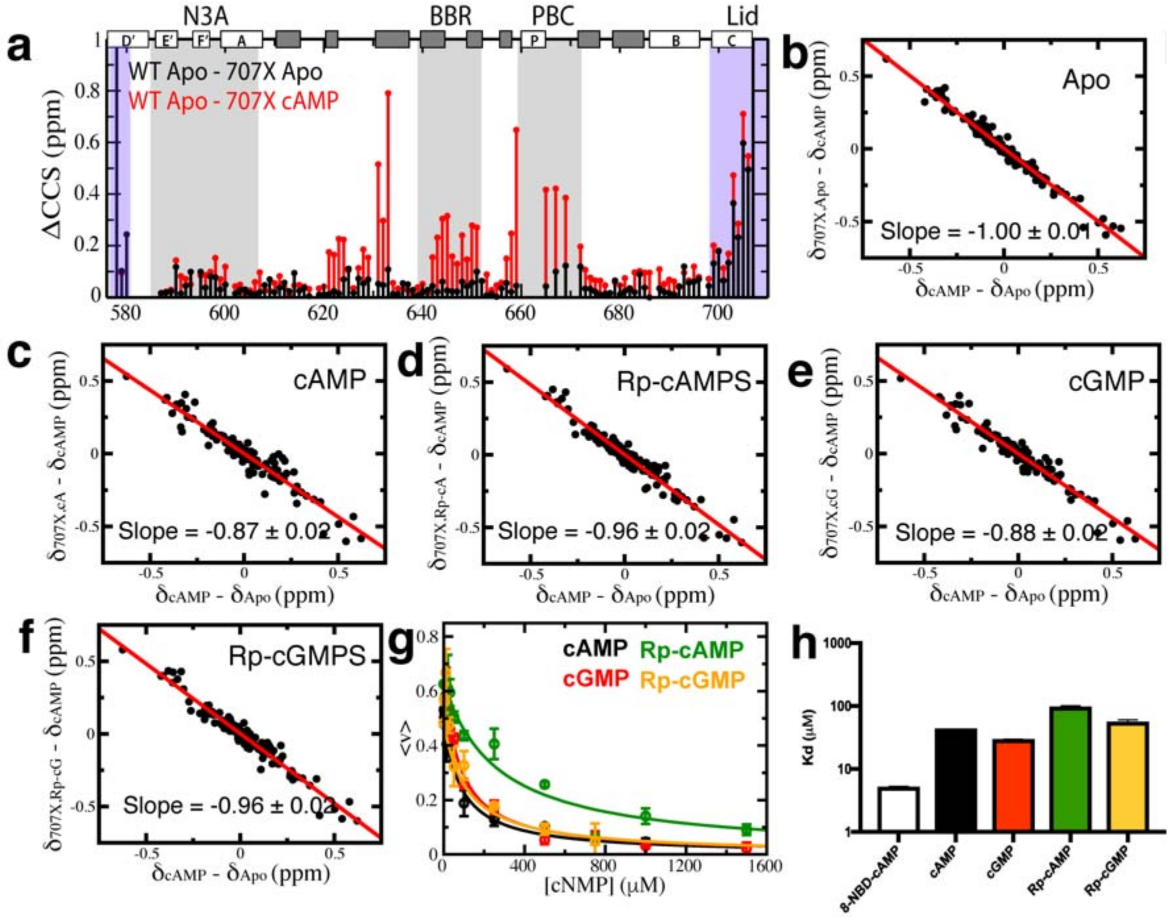

Figure S2. *Non-Additivity in the Rp/G Double-Ligand Cycle for the Inactive Lidless Mutant HCN4 707X.* **(a)** NH chemical shift differences between the apo WT and either the apo (black) or cAMP-bound (red) 707X construct (2). Regions highlighted in purple are sensitive to truncation effects. In the apo form, the lidless HCN4 707X construct remains quite similar to the untruncated HCN4 CNBD, and upon cAMP binding it exhibits only marginal chemical shift changes in the regions that are most sensitive to the inactive-to-active transition, such as the N3A and the B-helix. **(b-f)** Chemical shift correlation plots to determine the fractional activation of HCN4 707X either in the apo or cNMP-saturated forms, confirming that the lid truncation in HCN4 707X is effective in silencing the cNMP-induced 1-to-2 conformational change of the HCN4 CNBD. **(g)** Binding competition isotherms for the cNMP analogs in the Rp/G cycle *vs.* the fluorescent 8-NBD-cAMP ligand measured for the HCN4 707X construct at 5 μM in the case of cAMP and Rp-cGMPS and at 10 μM for the other cNMPs. **(h)** K_d values for the cAMP analogs in (g) shown as a log scale bar plot. The K_d of 8-NBD-cAMP was measured by direct titration. K_d values are also reported in Table S1.

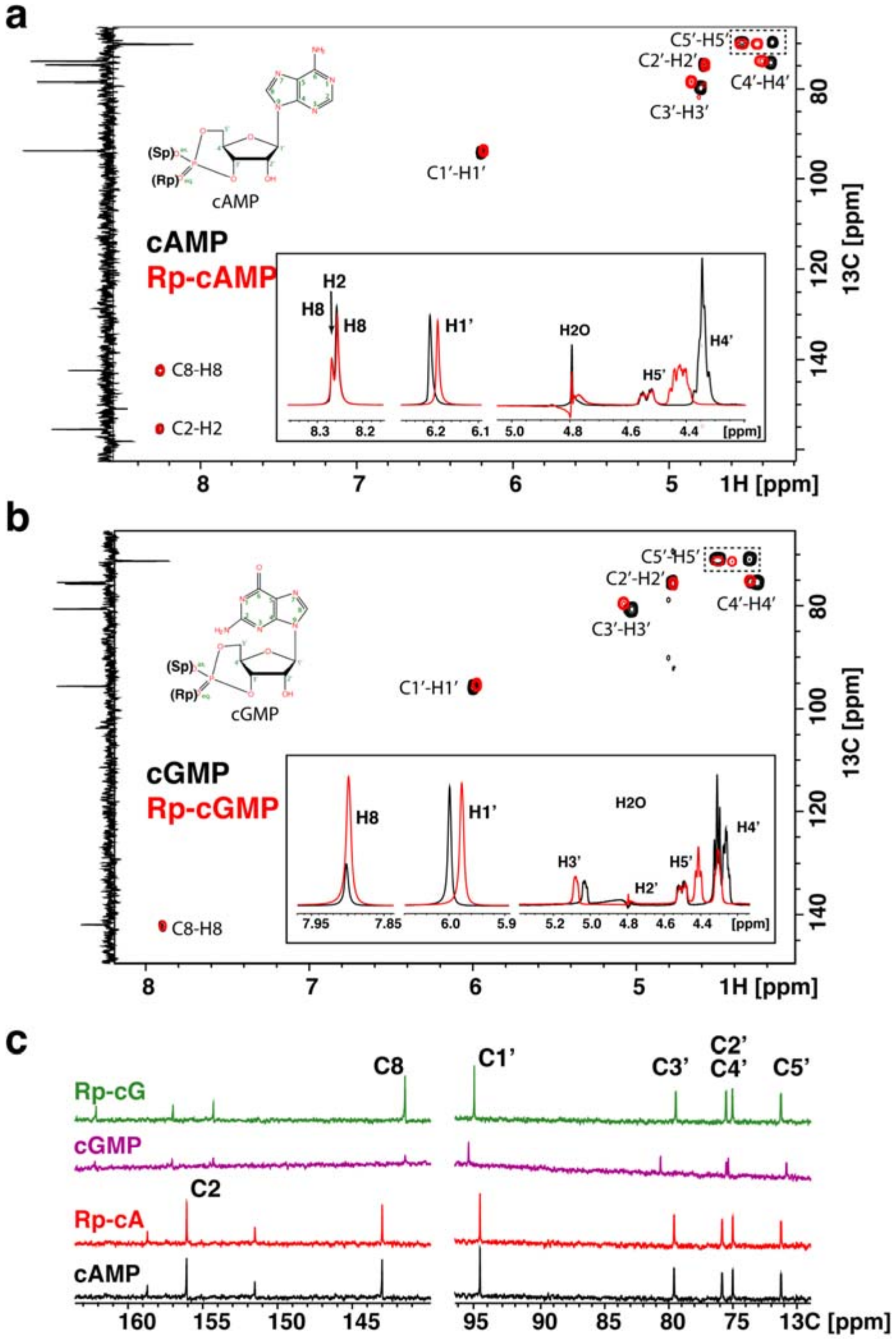

Figure S3. *Assessment of Intra-Ligand Covalent Cross-Talk between Substituents A and B through ^{1}H and ^{13}C Chemical Shifts of Unbound cNMPs*. {^{13}C,^{1}H}-HSQC spectra of cAMP **(a)** and cGMP **(b)** analogs. Along the left side of the HSQC spectra are ^{13}C DEPT experiments to highlight carbons that are covalently bonded to one or two hydrogens. For instance, the dashed box highlights the peaks of two protons bound to the 5' carbon atom. The inserts show close ups of ^{1}H peaks among the cyclic nucleotides. **(c)** 1D ^{13}C NMR spectra of the cNMPs in (a) and (b). No significant chemical shift variations are observed for the base upon introduction of the Rp substitution, pointing to negligible covalent cross-talk for the double-ligand cycle in Fig. 1c.

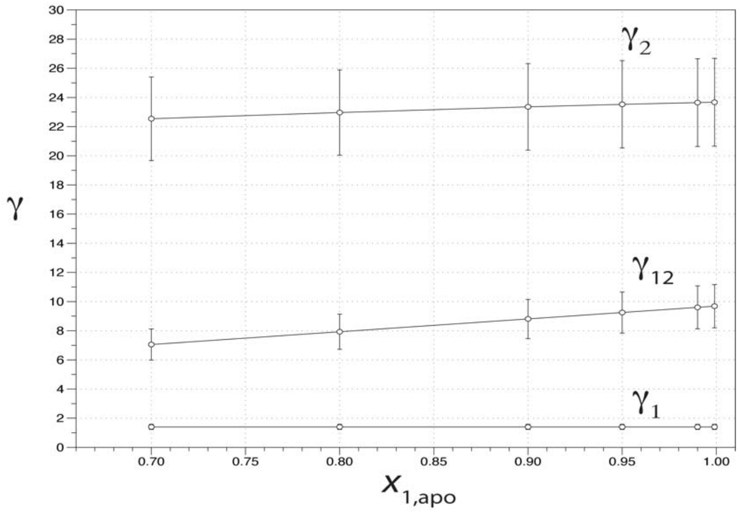

Figure S4. *Dependence of the State- and Transition-Specific γ Non-Additivity Factors on the State-Populations of the Apo Protein (P).* Rp/G double-ligand cycle. γ_{12} was computed using equation (3), while γ_1 and γ_2 were calculated using equations (5) and (6), respectively, based on the conversion of relative fractional shifts measured by NMR to absolute state-populations (Section 2). Most γ variations induced by changes in $x_{1,\text{apo}}$ are within experimental error, and the mechanistic conclusions based on γ_{12}, γ_1 and γ_2 are not affected by $x_{1,\text{apo}}$.

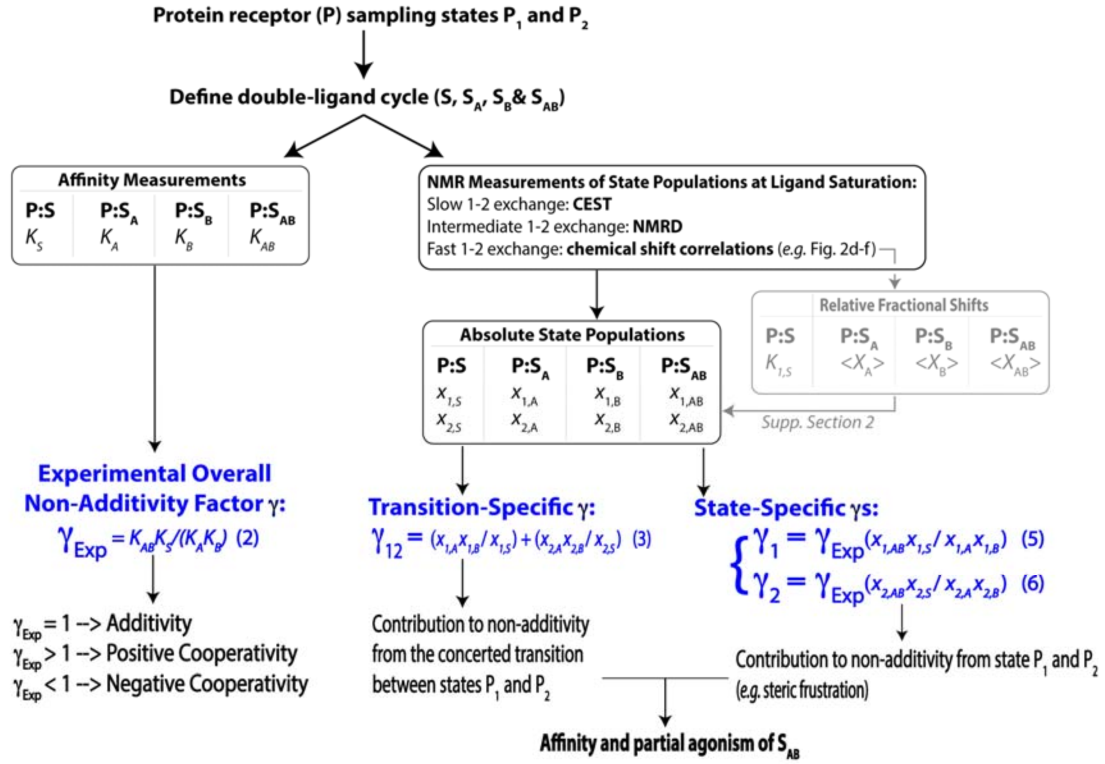

Figure S5. *Scheme for the Dissection of the Experimental Non-Additivity Factor (γ_{Exp}) into Transition- and State-Specific Components (γ_{12}, γ_1 and γ_2).* The experimental inputs include measurements of association constants for the four protein:ligand complexes that define the non-additivity cycle (P:S, P:S_A, P:S_B and P:S_{AB}), as well as the respective state-populations. The NMR methods utilized for measuring the latter depend on the 1 ⇔ 2 exchange kinetic regime. In the case of fast exchange, chemical shift correlation analyses provide the relative positions of the 1 ⇔ 2 equilibrium, *i.e.* the average fractional shifts of P in the presence of saturating amounts of S_A, S_B and S_{AB} relative to apo P and P:S. Such relative shifts are then converted into absolute populations (Section 2), which requires the affinity of ligand S for conformation P_1 (*i.e.* state-specific association constant $K_{1,S}$; grey box). Once these inputs are experimentally accessible, it is possible to calculate not only γ_{Exp}, but also the contribution to γ_{Exp} arising from the P_1 ⇔ P_2 transition, *i.e.* γ_{12} (the transition-specific γ), as well as from state-specific non-additivity, *i.e.* γ_1 and γ_2. Both transition- and state-specific γ values contribute to the affinity and partial agonism of S_{AB}.

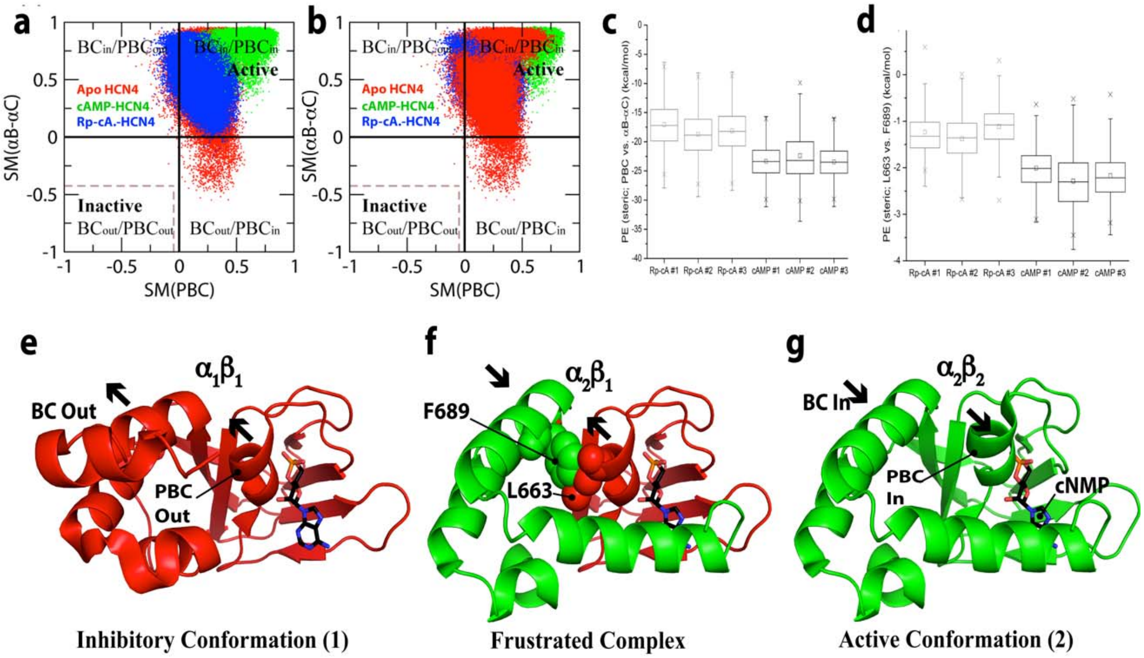

Figure S6. *MD Simulations of the HCN4 CNBD:Rp-cAMPS Complex.* **(a, b)** Two-dimensional plots of the computed P_2 *vs.* P_1 structure similarity measures (SM) for the B-C and PBC regions (3) in the HCN4 CNBD:Rp-cAMPS complex (blue) as well as the corresponding apo (red) and cAMP-bound (green) values from reference (3), shown here for the convenience of comparison. Panels a and b include the same data sets, but with a different order of front *vs.* back layers. **(c)** Distribution of potential energies of steric contact between the PBC and B-C structural elements. The PBC and B-C regions span residues 659-671 and 687-711 of HCN4, respectively. Steric potential energies were computed for three replicate simulations of the R_p-cAMPS-bound ("Rp-cA"; gray plots) and cAMP-bound ("cAMP"; black plots) monomeric states of the HCN4 IR. **(d)** As panel (c) but for the potential energies of steric contact between the PBC residue L663 and the B-helix residue F689. Statistics reported in each boxplot of panels (c) and (d) are as follows: the middle, bottom and top lines of the central box represent the median, 25th percentile and 75th percentile of the data set, respectively; the whiskers represent additional data falling within 1.5*IQR above the 75th percentile or below the 25th percentile (where IQR is the difference between the 75th and 25th percentiles); the "□" symbol represents the mean of the data set; and the two "×" symbols represent the 1st and 99th percentiles of the data set. **(e-g)** Hypothesis on the HCN4 WT frustration. The HCN4 CNBD samples both inhibitory (panel e: red, 1, apo HCN4 CNBD, PDB code 2MNG) and active (panel g: green, 2, cAMP-bound HCN4 CNBD, PDB code 3OTF) conformations, in which the α- and β-subdomains are both either in the P_1 or P_2 state (*i.e.* $\alpha_1\beta_1$ or $\alpha_2\beta_2$). However, when Rp-cAMPS binds to the HCN4 CNBD, steric hindrance arises between L663 in the PBC and F689 in the B helix. Arrows indicate the in/out movement of the B-C and PBC helices upon cNMP-binding.

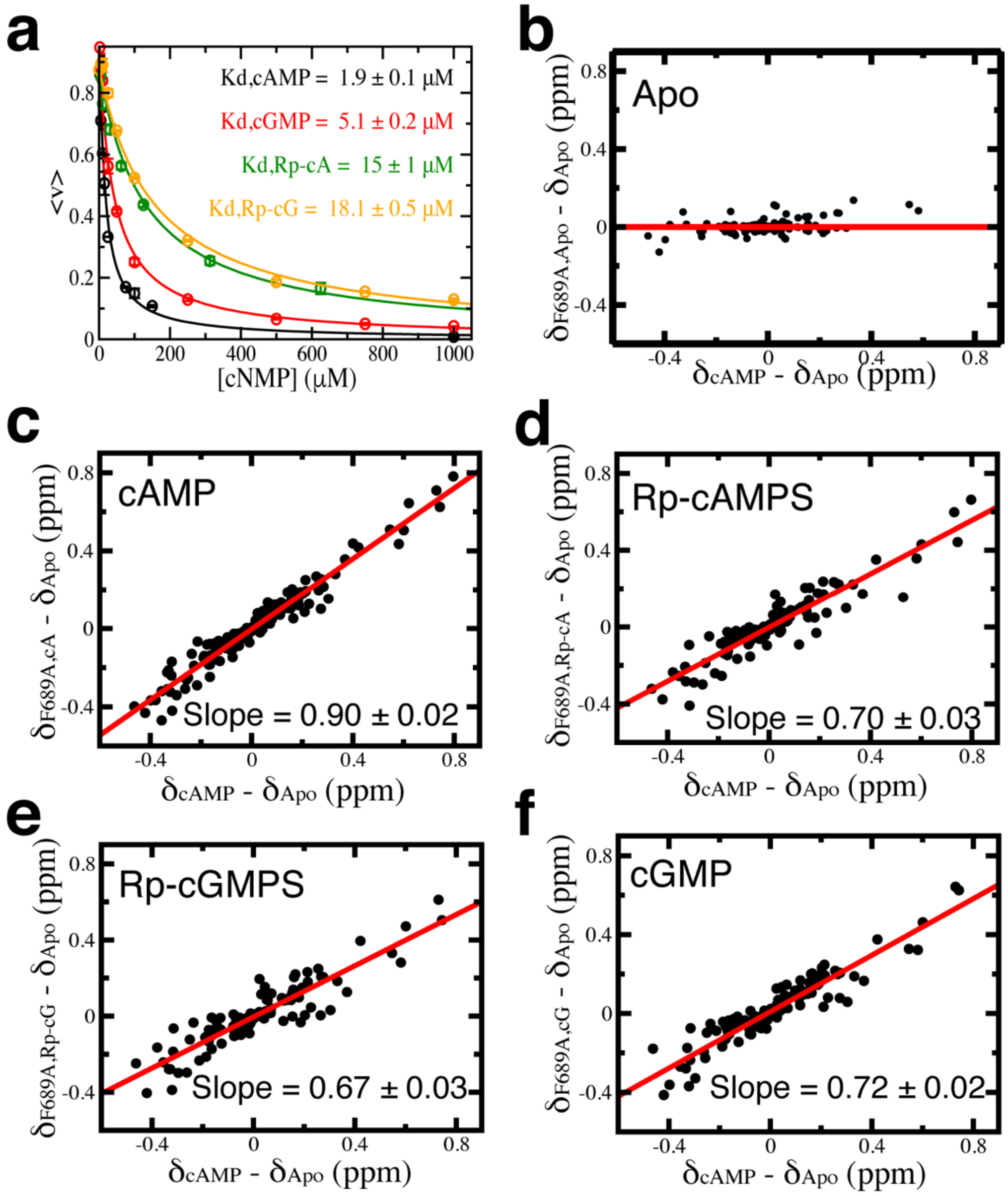

Figure S7. *Fractional Equilibrium Shifts $\langle X_j \rangle$ and Affinities for the Rp / G Double-Ligand Cycle as Applied to the F689A HCN4 (563-724) mutant.* **(a)** 8-NBD-cAMP fluorescence competition isotherms similar to those in Fig. 2a, but measured for F689A HCN4 (563-724). **(b-f)** Chemical shift correlation plots similar to Fig. 2d-f, but for the F689A HCN4 (563-724) mutant. If not otherwise specified, chemical shifts refer to WT HCN4 (563-724). The $\langle X_j \rangle$ values and affinities are compiled in Table S1.

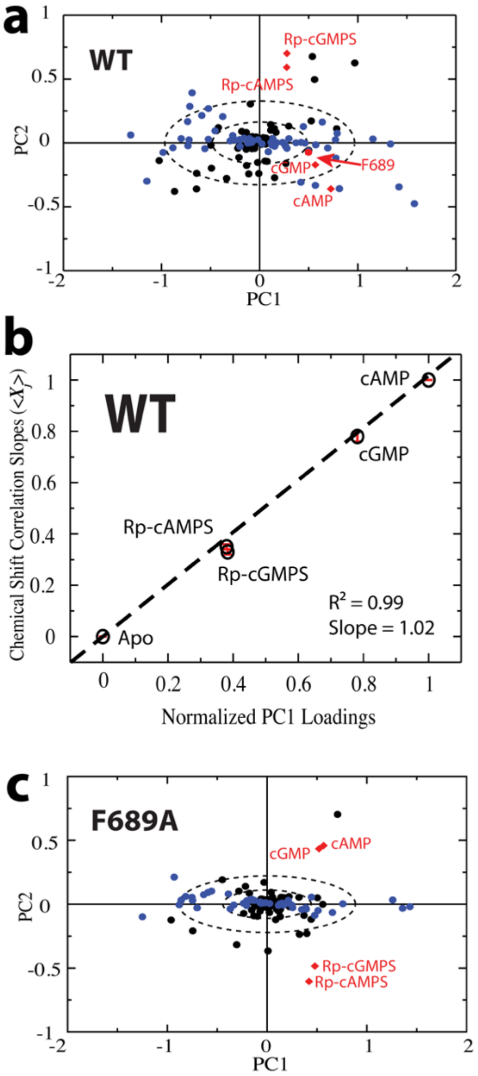

Figure S8. **(a)** CHESCA SVD analysis for WT HCN4 (563-724) using the apo sample as a chemical shift reference. The first two principal components (PC1 and PC2) alone account for 96.4% of the total variance. Scores are shown as circles, while the loadings are shown as red diamonds. The single linkage allosteric cluster in Fig. 4c is shown as blue circles. The score of F689 is highlighted in red. One and two standard deviation ellipsoids for PC1 and PC2 are shown as dashed lines. **(b)** *Correlation between SVD PC1 CHESCA Loadings and Chemical Shift Correlation Slopes (<X_j> Fractional Activations)*. Plot of slopes from Fig. 2d-f *vs.* the corresponding SVD PC1 loading values from panel (a) normalized with respect to cAMP. Both approaches provide comparable fractional shifts relative to the cAMP-bound and apo WT HCN4 CNBD samples. This result implies that PC1 reports primarily on allostery. Hence, the PC1 score for F689 in the vicinity of the ellipsoid corresponding to one-standard deviation (a) points to a major allosteric role for F689. **(c)** As (a), but for the F689A HCN4 (563-724) mutant. The first two principal components (PC1 and PC2) alone account for 96.2% of the total variance.

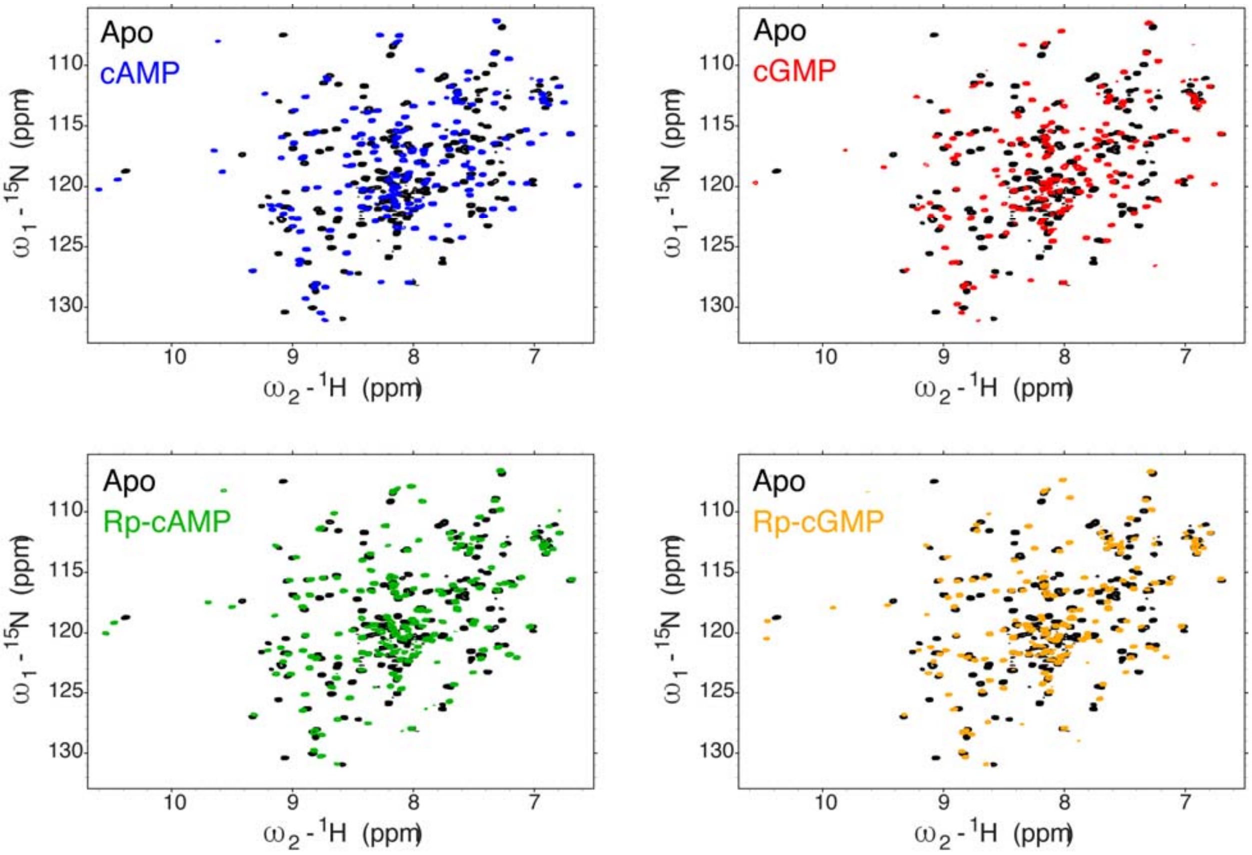

Figure S9. *Complete HSQC spectra for WT HCN4 (563-724) in the unbound or cyclic nucleotide bound forms*. Cyclic nucleotides are from the double-ligand cycle of Fig. 1c. Color coding is shown in each panel. The apo and cAMP-bound HSQC spectra were originally reported in supplementary reference 5 and are included here for the convenience of comparison.

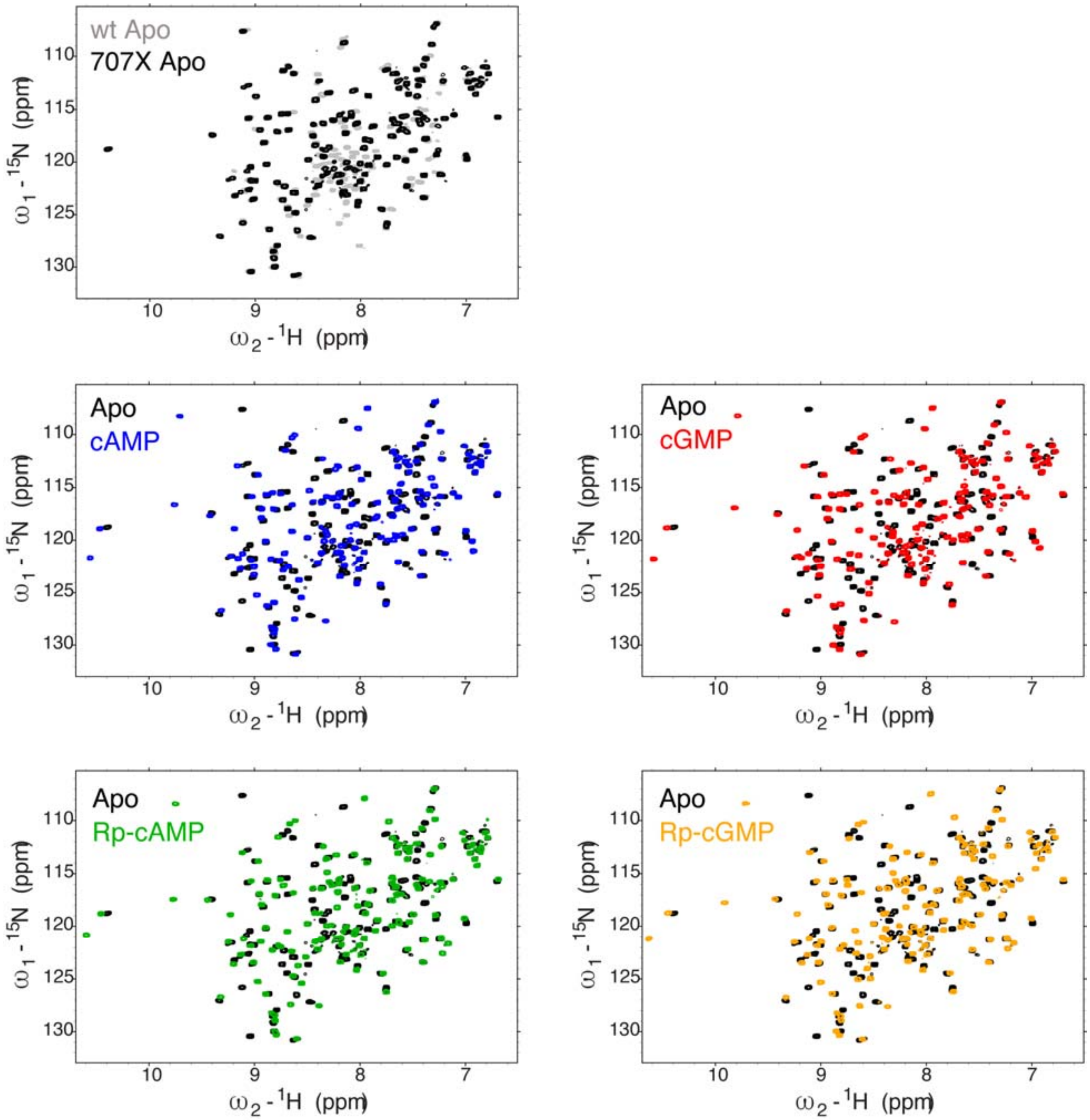

Figure S10. *Complete HSQC spectra for 707X HCN4 in the unbound* (15) *or cyclic nucleotide bound forms*. Cyclic nucleotides are from the double-ligand cycle of Fig. 1c. Color coding is shown in each panel.

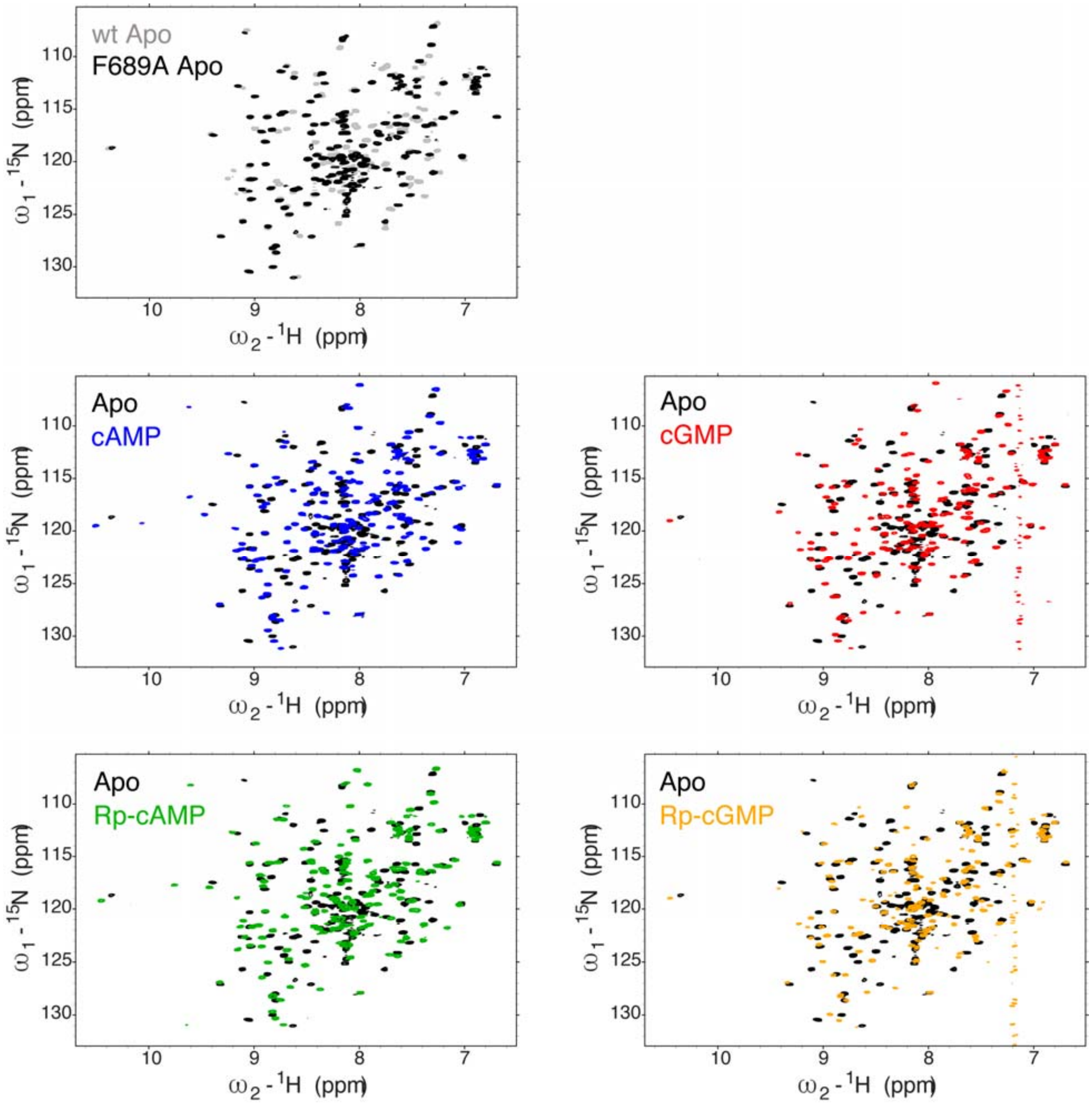

Figure S11. *Complete HSQC spectra for F689A HCN4 (563-724) in the unbound or cyclic nucleotide bound forms*. Cyclic nucleotides are from the double-ligand cycle of Fig. 1c. Color coding is shown in each panel.

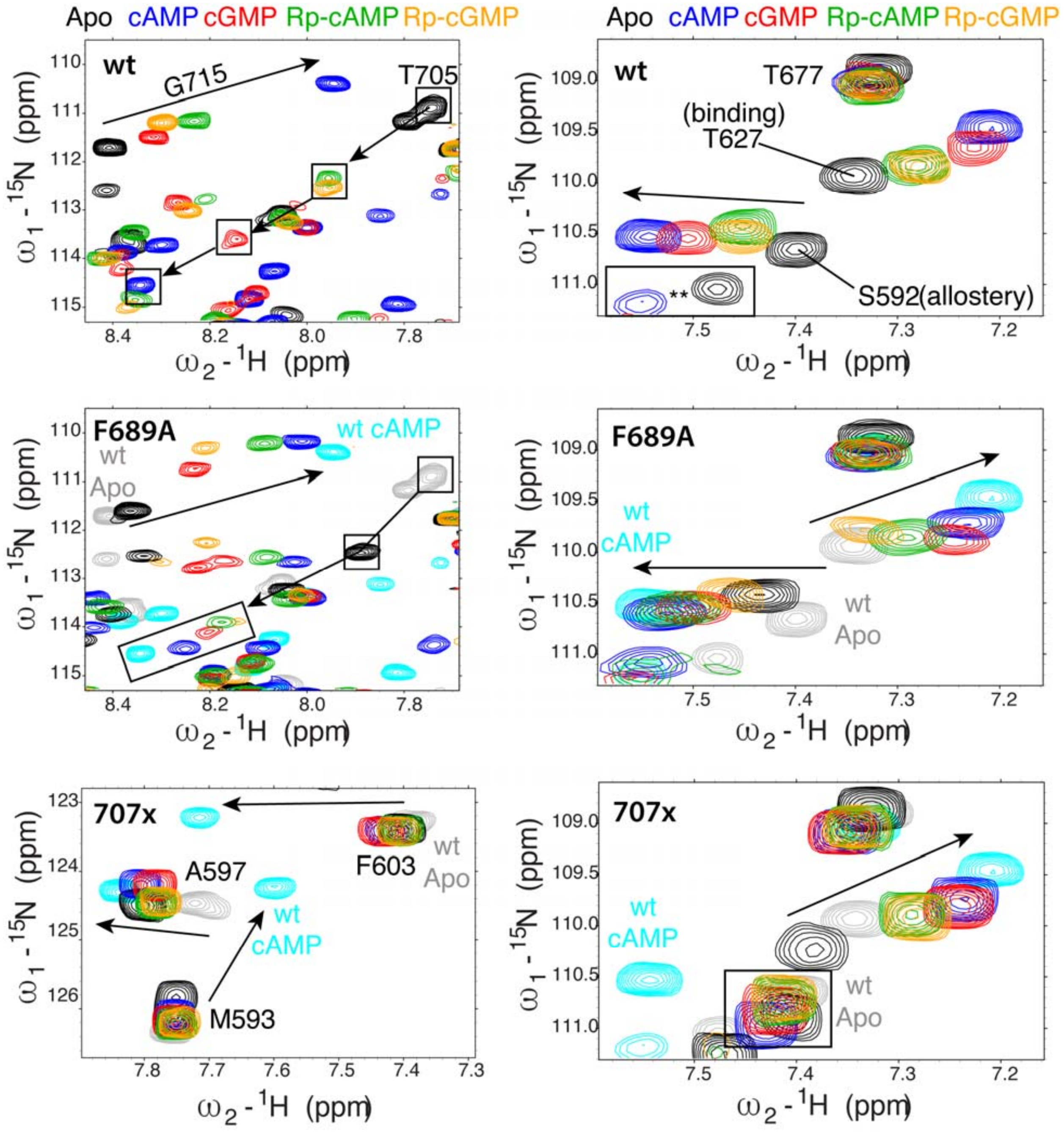

Figure S12. *Zoomed-in expansions from the HSQC spectra in Figures S9-S11*. Cross-peaks of selected residues sensing binding or allosteric changes are labeled.

Table S1. *Ligand Affinities, Fractional Activations and Decomposition of the Experimental Value (γ_{Exp}) into State-Specific (γ_1 and γ_2) and Transition-Specific (γ_{12}) Contributions for the Rp/G Cycle*

Double Ligand Cycle		**HCN4_CNBD WT**		**HCN4_CNBD 707X**			**HCN4_CNBD F689A**	
		K_d /μM [a]	$< X_j >$ [b]	**K_d /μM** [a]	$\frac{x_{1,Sj,Mt}}{x_{1,Apo,Mt}}$ [b]	**$K_{d,1}$ /μM** [c]	**K_d /μM** [a]	$< X_j >$ [b]
S	**cAMP**	0.80 ± 0.02	1	43.0 ± 0.8	0.87 ± 0.02	49.4 ± 1.5	1.9 ± 0.1	0.90 ± 0.02
S_A	**cGMP**	8.2 ± 0.5	0.78 ± 0.02	29.1 ±0 .6	0.88 ± 0.02	33.1 ± 1.0	5.1 ± 0.2	0.72 ± 0.02
S_B	**Rp-cAMPS**	107 ± 5	0.35 ± 0.01	96 ± 5	0.96 ± 0.02	100 ± 6	15.0 ± 1.0	0.70 ± 0.03
S_{AB}	**Rp-cGMPS**	56 ± 2	0.33 ± 0.01	55 ± 5	0.96 ± 0.02	57 ± 5	18.1 ± 0.5	0.67 ± 0.03
	$< X_{AB,12} >$		0.02 [d]					0.44 [d]
Rp/G	γ_{Exp}	19.6 ± 1.7		1.2 ± 0.1		1.2 ± 0.1	2.2 ± 0.2[e]	
	γ_{12}	9.6 ± 0.7 [d]					1.4 ± 0.1[e]	
	γ_1	1.4 ± 0.2					0.9 ± 0.1[e]	
	γ_2	23.6 ± 3.0 [d]					2.7 ± 0.5[e]	

[a] Measured through fluorescence competition with 8-NBD-cAMP (K_d = 0.73 ± 0.03 μM). The HCN4_CNBD construct is HCN4 (563-724). [b] Computed based on the chemical shift correlations of Fig. 2d-f for wt, Fig. S2b-f for 707X and S7c-f for F689A, which are in turn based on the NMR spectra shown in Fig. S9-S12. [c] Computed as explained in supplementary reference (2). [d] Computed assuming $x_{1,Apo} = 0.99$. Similar results are obtained with different $x_{1,Apo}$ values (Fig. S4). [e] Computed using a β value obtained through equation (S2) and by normalizing the $< X_j >$ values to $< X_{cAMP} >$.

Table S2. *Gibbs Free Energy of Coupling between Mutated Protein Sites and Specific Ligand Substituents*

		$\Delta G_{\text{mutated site/ligand substituent coupling}}$ / (kcal/mol)*	
Ligand Substitution		**HCN4_CNBD 707X**	**HCN4_CNBD F689A**
S_A	**cGMP**	1.62 ± 0.04	0.80 ± 0.04
S_B	**Rp-cAMPS**	2.44 ± 0.05	1.67 ± 0.06

*Computed based on the thermodynamic cycle of Fig. S1c as: $\Delta G_{\text{mutated site/ligand substituent coupling}} = -RT \ln (K_{d,WT,cA} K_{d,MT,cA'} / K_{d,MT,cA} K_{d,WT,cA'})$ using T = 300 K and the dissociation constants in Table S1. MT stands for protein mutation and cA' for cAMP substitution.

Supporting References

1. Dill, Ken A. and Bromberg, S. 2003. Molecular Driving Forces: Statistical Thermodynamics in Chemistry and Biology. New York: Garland Science.
2. Moleschi, K.J., M. Akimoto, and G. Melacini. 2015. Measurement of State-Specific Association Constants in Allosteric Sensors through Molecular Stapling and NMR. *J. Am. Chem. Soc.* 137.
3. VanSchouwen, B., M. Akimoto, M. Sayadi, F. Fogolari, and G. Melacini. 2015. Role of Dynamics in the Autoinhibition and Activation of the Hyperpolarization-activated Cyclic Nucleotide-modulated (HCN) Ion Channels. *J. Biol. Chem.* 290:17642–17654.
4. Das, R., and G. Melacini. 2007. A model for agonism and antagonism in an ancient and ubiquitous cAMP-binding domain. *J. Biol. Chem.* 282:581–593.
5. Akimoto, M., Z. Zhang, S. Boulton, R. Selvaratnam, B. VanSchouwen, M. Gloyd, E.A. Accili, O.F. Lange, and G. Melacini. 2014. A mechanism for the auto-inhibition of hyperpolarization-activated cyclic nucleotide-gated (HCN) channel opening and its relief by cAMP. *J. Biol. Chem.* 289:22205–20.